JGR Solid Earth

RESEARCH ARTICLE
10.1029/2023JB027699

High-Temperature Deformation of Enstatite-Olivine Aggregates

M. Bystricky[1], J. Lawlis[2], S. Mackwell[3], and F. Heidelbach[4]

[1]Institut de Recherche en Astrophysique et Planétologie, UPS, CNRS, CNES, Université de Toulouse, Toulouse, France, [2]Department of Geosciences, Pennsylvania State University, University Park, PA, USA, [3]Department of Geology, University of Maryland, College Park, MD, USA, [4]Bayerisches Geoinstitut, Universität Bayreuth, Bayreuth, Germany

Key Points:

- Polycrystalline samples of enstatite and olivine with different volumetric ratios were deformed in compression at high temperature
- All two-phase aggregates have strengths in dislocation creep that lie between the uniform stress and uniform strain rate bounds
- In dislocation creep the flow law for olivine provides a good estimate of the viscosity of olivine-pyroxene rocks under natural conditions

Supporting Information:

Supporting Information may be found in the online version of this article.

Correspondence to:

M. Bystricky,
mbystricky@irap.omp.eu

Citation:

Bystricky, M., Lawlis, J., Mackwell, S., & Heidelbach, F. (2024). High-temperature deformation of enstatite-olivine aggregates. *Journal of Geophysical Research: Solid Earth*, *129*, e2023JB027699. https://doi.org/10.1029/2023JB027699

Received 21 AUG 2023
Accepted 22 FEB 2024

Author Contributions:

Conceptualization: J. Lawlis, S. Mackwell
Data curation: M. Bystricky, S. Mackwell, F. Heidelbach
Formal analysis: M. Bystricky, J. Lawlis, S. Mackwell, F. Heidelbach
Funding acquisition: S. Mackwell
Investigation: M. Bystricky, J. Lawlis, F. Heidelbach
Methodology: M. Bystricky, J. Lawlis, S. Mackwell
Project administration: J. Lawlis, S. Mackwell
Resources: S. Mackwell
Software: M. Bystricky, J. Lawlis, S. Mackwell
Supervision: S. Mackwell

Abstract Synthesized polycrystalline samples composed of enstatite and olivine with different volumetric ratios were deformed in compression under anhydrous conditions in a Paterson gas-medium apparatus at 1150–1300°C, an oxygen fugacity buffered at Ni/NiO, and confining pressures of 300 or 450 MPa (protoenstatite or orthoenstatite fields). Mechanical data suggest a transition from diffusion to dislocation creep with increasing differential stress for all compositions. Microstructural analyses by optical and scanning electron microscopy reveal well-mixed aggregates and homogeneous deformation. Crystallographic preferred orientations measured by electron backscatter diffraction are consistent with activation of the slip systems (010)[100] and (010)[001] for olivine and (100)[001] and (010)[001] for enstatite, as expected at these conditions. Nonlinear least-squares fitting to the full data set from each experiment allowed the determination of dislocation creep flow laws for the different mixtures. The stress exponent is 3.5 for all compositions, and the apparent activation energies increase slightly as a function of enstatite volume fraction. Within the limits of experimental uncertainties, all two-phase aggregates have strengths that lie between the uniform strain rate (Taylor) and the uniform stress (Sachs) bounds calculated using the dislocation creep flow laws for olivine and enstatite. Calculation of the Taylor and Sachs bounds at strain rate and temperature conditions expected in nature (but not extrapolating in pressure) indicates that using the dislocation creep flow law for monomineralic olivine aggregates provides a good estimate of the viscosity of olivine-orthopyroxene rocks deforming by dislocation creep in the deeper lithosphere and asthenosphere.

Plain Language Summary The rheology of Earth's upper mantle is generally modeled using mechanical flow laws determined for aggregates composed only of olivine minerals, in spite of the polyphase nature of mantle rocks. In this study, we investigated the effect of phase volume proportions on the high-temperature deformation properties of aggregates composed of the two most abundant minerals in the upper mantle, olivine and enstatite. The samples were deformed under dry conditions in triaxial compression at 1150–1300°C, under oxygen fugacity fixed at the Ni/NiO solid buffer, and confining pressures of 300 or 450 MPa, at conditions where enstatite has two different crystallographic structures. At both pressures, in the dislocation creep regime, where deformation occurs mostly by the motion of dislocations along slip planes within mineral grains, the strengths of all the two-phase mixtures lie between the uniform strain rate and the uniform stress bounds, which assume iso-strain and iso-stress conditions, respectively, in all the grains comprising each aggregate. Extrapolating these bounds to temperatures and strain rates expected in nature indicates that the viscosity of mantle rocks can be modeled adequately with the dislocation creep flow law for olivine.

1. Introduction

Flow within Earth and other terrestrial bodies in the solar system is a critical part of the heat engine of each planet and occurs through solid-state deformation of the rocks that comprise their interiors. In modeling the flow properties of a planet, it is optimal to use actual rheologies for the appropriate rocks that exist under the thermomechanical conditions for a given depth within the body (e.g., Hirth & Kohlstedt, 2003; Kirby & Kronenberg, 1987; Kohlstedt et al., 1995). Unfortunately, this is not always possible as flow in planetary bodies usually occurs at rates that are much slower than is achievable in the laboratory, and extrapolation from laboratory conditions to planetary interiors is not straightforward (e.g., Hirth & Kohlstedt, 2015; Paterson, 1987; Paterson, 2001). It is for instance possible that deformation mechanisms identified in the laboratory, such as dislocation creep, diffusion creep or grain boundary sliding, may not be appropriate under deep planetary interior conditions. Nonetheless, microstructural analyses of natural rocks and mantle seismic anisotropy data provide strong

Validation: M. Bystricky, S. Mackwell, F. Heidelbach
Visualization: M. Bystricky, S. Mackwell, F. Heidelbach
Writing – original draft: M. Bystricky, J. Lawlis, S. Mackwell, F. Heidelbach
Writing – review & editing: M. Bystricky, S. Mackwell, F. Heidelbach

evidence of the ubiquitous presence of crystallographic preferred orientations (CPO) of olivine in lithosphere and asthenosphere rocks (e.g., Nicolas & Christensen, 1987; Mainprice & Silver, 1993; Ben Ismail & Mainprice, 1998; Montagner, 1998; Smith & Eckström, 1999; Silver et al., 1999; Tommasi & Vauchez, 2015; and references therein). CPOs are predominantly created by dislocation glide processes, implying that dislocation creep, where deformation occurs mostly by the motion of dislocations along slip planes within mineral grains, is an important deformation mechanism. In many studies of mantle rocks, olivine CPOs are consistent with deformation by dislocation creep (e.g., Baptiste et al., 2015; Zaffarana et al., 2014). In addition, geodynamic modeling of seismic anisotropy points to dislocation creep as the likely dominant deformation mechanism in the uppermost mantle (e.g., Asaadi et al., 2011; Becker et al., 2008; van Hunen et al., 2005) and possibly also in the deep upper mantle despite decreasing seismic anisotropy with depth (Mainprice et al., 2005).

A further complication to extrapolation of laboratory rheologies to natural conditions results from the polyphase nature of rocks in planetary interiors. Experimental rheologies have been measured for single-phase aggregates of two major minerals in Earth's upper mantle: olivine (dunite) (e.g., Carter & Avé Lallemant, 1970; Chopra & Paterson, 1981, 1984; Zeuch & Green, 1984; Karato et al., 1986; Borch & Green, 1989; Hirth & Kohlstedt, 1995a, b; Bystricky et al., 2000; Mei & Kohlstedt, 2000a,b; Karato & Jung, 2003; Durham et al., 2009; Keefner et al., 2011; Hansen et al., 2011; Faul et al., 2011; Ohuchi et al., 2017; Dixon & Durham, 2018; and references therein), and orthopyroxene (enstatite) (Raleigh et al., 1971; Ross & Nielsen, 1978; Hitchings et al., 1989; Bystricky et al., 2016; Zhang et al., 2017, 2020; and references therein). Since olivine is the most abundant and arguably weakest phase within the deep lithosphere and asthenosphere on Earth, it is often assumed that single-phase olivine-aggregate rheologies provide a good first-order approximation to creep within these regions (e.g., Kirby & Kronenberg, 1987; Kohlstedt et al., 1995). However, there have been few studies on the influence on mantle rheology of one or more of the dominant secondary phases in Earth's mantle: orthopyroxene, clinopyroxene and garnet. A number of experimental studies have been performed for olivine-enstatite aggregates in the diffusion creep field (Ji et al., 2001; McDonnell et al., 2000; Soustelle & Manthilake, 2017; Sundberg & Cooper, 2008; Tasaka et al., 2013), dislocation-accommodated grain-boundary sliding field (for iron-rich olivine-enstatite aggregates: Tasaka et al., 2017, 2020) and in the dislocation creep field (Hitchings et al., 1989). Deformation studies have also been conducted on olivine-diopside aggregates in the diffusion creep field (Précigout & Stünitz, 2016; Zhao et al., 2019). Within the dislocation creep field expected for the lithosphere and asthenosphere on Earth, only the Hitchings et al. (1989) study provides significant insight into the effect of enstatite content on aggregate behavior in dislocation creep. Unfortunately, their work represents only a preliminary study and does not provide a systematic investigation of the behavior sufficient to constrain models for extrapolation to Earth's interior.

The present study of enstatite-olivine two-phase deformation builds on the previous report by Bystricky et al. (2016) on the rheology of enstatite aggregates in the protoenstatite and orthoenstatite fields. That study determined flow laws for dislocation creep and demonstrated that, under similar conditions (other than confining pressure), protoenstatite is stronger by a factor of about 2 in stress than orthoenstatite. As the study by Bystricky et al. (2016) was essentially identical in sample preparation and deformation conditions, it provides the end-member enstatite constraint on our study of two-phase behavior of enstatite-olivine aggregates.

2. Materials and Methods

2.1. Starting Material

Olivine powders were produced from optically clear olivine single crystals from San Carlos, Arizona $(Mg_{0.91}Fe_{0.09})_2SiO_4$, that were carefully hand-selected to exclude accessory minerals such as spinel or pyroxene. These crystals were broken into millimeter-size fragments in a steel crusher, ground using an agate mortar and pestle, and sieved to yield grain sizes below 45 μm. Gravitational settling of the powders in distilled water allowed separation of powders into 2 bins with mean grain sizes of 30 ± 10 μm (coarse) and 8 ± 3 μm (fine).

Enstatite was produced by reacting the olivine powders with fine-grained quartz, as described in detail in Bystricky et al. (2016). Equal molar ratios of olivine and quartz powders were ground in distilled water using a micronizing mill to grain sizes less than 10 μm. They were then reacted in an olivine crucible at 1430°C for 150 hr in a one-atm furnace under controlled oxygen fugacity conditions near Ni/NiO ($10^{-5.5}$ atm) using CO/CO_2 gas mixtures. The powders were subsequently reground and reacted a second time under the same conditions for an additional 100 hr to ensure that the reaction was complete. As for the olivine material, these reacted powders were

Table 1
Experimental Conditions for Hot-Pressing Enstatite-Olivine Aggregates

Exp.	Composition (vol%)	P_c (MPa)	T (°C)	t (h)	d_h (En) (μm)	d_h (Ol) (μm)
PI-339[a]	100%En	300	1300	6	10.0 ± 0.7	n/a
PI-402[a]	100%En	300	1300	2	–	n/a
PI-400	75%En-25%Ol	300	1300	2	–	-
PI-458	75%En-25%Ol	300	1300	8	11.9 ± 1.0	11.7 ± 2.0
PI-343	50%En-50%Ol	300	1300	5	5.6 ± 0.5	6.6 ± 0.5
PI-450	50%En-50%Ol	300	1300	8	–	–
PI-399	25%En-75%Ol	300	1300	2	–	–
PI-453	25%En-75%Ol	300	1300	8	9.8 ± 1.0	13.2 ± 1.3
PI-512[a]	100%En	450	1300	12	–	n/a
PI-539[a]	100%En	450	1300	8	–	n/a
PI-560	75%En-25%Ol	450	1300	8	5.9 ± 0.1	14.3 ± 1.6
PI-561	50%En-50%Ol	450	1300	8	–	–
PI-541	40%En-60%Ol	450	1300	4	8.3 ± 0.5	6.7 ± 0.1
PI-553	25%En-75%Ol	450	1300	8	–	–

Note. P_c is confining pressure, T is temperature and t is the duration of the hot-press; d_h is the average grain size after the hot-press; errors on d_h are 2σ. [a]Samples are from Bystricky et al. (2016).

ground and gravitationally settled to provide grain-size ranges similar to the olivine powders. Microprobe analysis showed that the resulting enstatite powders were homogeneous with a composition near En_{91}. X-ray powder diffraction analysis confirmed that the crystalline structure for the enstatite powders was monoclinic (low clinoenstatite). Both olivine and enstatite powders were stored in a vacuum oven at 150°C to minimize water contamination prior to hot-pressing.

2.2. Sample Fabrication

Powders of enstatite (En) and olivine (Ol) were weighed on a microbalance to generate samples with the following volumetric ratios: 75%En-25%Ol, 50%En-50%Ol, 40%En-60%Ol, and 25%En-75%Ol (Table 1). After mechanical mixing for 2 hr, the powders for each sample were cold-pressed at a uniaxial stress of 200 MPa in a nickel sleeve (10 mm inner diameter, 20 mm long) with a hardened steel cold-pressing die. The nickel-jacketed cold-pressed samples were hot-pressed in an internally heated gas-medium pressure vessel for 2–12 hr at 1300°C and a confining pressure of 300 MPa (for experiments in the protoenstatite stability field) or 450 MPa (for experiments in the orthoenstatite stability field) (Table 1).

Porosities in the hot-pressed samples, measured using the Archimedean method, were less than 2%. Samples were cored to a uniform diameter of 8 mm and ground to a length of 14–16 mm for the deformation experiments. In order to remove any hydrous species that may have been trapped during the hot-pressing stage, the samples were subsequently annealed for 20 hr at 1000°C under controlled oxygen fugacity conditions near Ni/NiO in a one-atm furnace. A thin slice from each hot-press was kept for microstructural and infrared analysis. The infrared analysis, performed using an FTIR at The Pennsylvania State University, detected no O-H related infrared bands in the spectra of the hot-pressed samples at a resolution of 10 H/10^6 Si. Samples were stored in a vacuum oven at 150°C prior to the deformation experiments.

2.3. Deformation Apparatus and Experiments

The creep experiments were performed under constant load conditions in triaxial compression using a Paterson gas-medium deformation apparatus at the University of Minnesota (Paterson, 1990), courtesy of Prof. David Kohlstedt. In this apparatus, samples are heated using an internal furnace, with thermal gradients of <1°C/mm and <4°C over the entire hot zone of the furnace at all temperatures (up to 1300°C). The applied load was measured with an internal load cell, yielding differential stresses ($\sigma = \sigma_1 - \sigma_3$) accurate to ±2 MPa. Sample strains were

Table 2
Experimental Conditions for Creep of Enstatite-Olivine Aggregates

Exp.	Composition (vol%)	P_c (MPa)	T range (°C)	σ range (MPa)	ε_{tot} (%)	d (En) (μm)	d (Ol) (μm)
PI-339[a]	100%En	300	1250–1300	65–244	14	6.9 ± 0.3	n/a
PI-402[a]	100%En	300	1299	26–223	8	7.3 ± 0.2	n/a
PI-400	75%En-25%Ol	300	1200–1297	85–229	11.8	8.7 ± 0.4	6.3 ± 0.6
PI-458	75%En-25%Ol	300	1200–1297	226–232	7.4	–	–
PI-343	50%En-50%Ol	300	1244–1300	40–260	19.1	7.3 ± 0.4	7.8 ± 0.4
PI-450	50%En-50%Ol	300	1279–1304	52–114	5.1	–	–
PI-455[b]	50%En-50%Ol	300	1175–1296	222–226	10.3	–	–
PI-399	25%En-75%Ol	300	1200–1300	55–229	17.9	7.0 ± 0.5	7.6 ± 0.3
PI-453	25%En-75%Ol	300	1300	54–108	3.5	8.0 ± 0.7	14.7 ± 1.1
PI-454[c]	25%En-75%Ol	300	1183–1300	221–223	6.5	8.0 ± 0.7	14.7 ± 1.1
PI-512[a]	100%En	450	1200–1275	170–430	23	11 ± 3	n/a
PI-539[a]	100%En	450	1200–1250	111–460	21	–	n/a
PI-560	75%En-25%Ol	450	1150–1250	279–421	15.6	–	–
PI-561	50%En-50%Ol	450	1150–1200	280–396	9.5	–	–
PI-541	40%En-60%Ol	450	1200–1250	54–401	18.6	–	–
PI-553	25%En-75%Ol	450	1225–1250	49–171	11.0	–	–

Note. P_c is confining pressure; "T range" and "σ range" are the ranges of temperatures and differential stresses visited during deformation; ε_{tot} is the total strain achieved; d is the average grain size after deformation; errors on d are 2σ. [a]Samples are from Bystricky et al. (2016). [b]Further deformation of sample PI-450. [c]Further deformation of sample PI-453; we assume the final grain sizes for PI-453 are the same as was measured for PI-454.

calculated from piston displacement, which was measured using a linear variable differential transducer external to the pressure vessel.

For each deformation experiment, a dry hot-pressed sample was taken from the vacuum oven, coated with NiO powder (to buffer oxygen fugacity at Ni/NiO), and placed in a nickel jacket (outer diameter 10 mm, inner diameter 8 mm). Thin nickel foil discs were placed at each end of the sample to prevent chemical interactions with the pistons. The jacketed sample was placed in a piston assembly comprising alumina and zirconia pistons surrounded by an outer iron sleeve (Paterson, 1990; Paterson & Chopra, 1982).

Once the sample assembly was loaded into the deformation apparatus, pressure was increased in 10–15 MPa increments to 300 or 450 MPa. Temperature was raised to the experimental conditions at ∼1°C/s once the pressure exceeded 100 MPa. After the pressure and temperature conditions for the experiment were reached, the sample was allowed to equilibrate for at least 2 hr prior to starting deformation.

Deformation experiments were performed as constant-load stepping tests at temperatures from 1150 to 1304°C and confining pressures of either 300 or 450 MPa, as delineated in Table 2. The applied loads were chosen to ensure that the resulting differential stresses did not exceed the confining pressure, minimizing crack nucleation and propagation. Measured strain rates ranged from 4.5×10^{-7} s^{-1} to 1.1×10^{-4} s^{-1}.

In each deformation step, the applied load was held constant until a quasi-steady-state regime was achieved, typically after a strain of at least 0.5%, as illustrated in Figure S1 in Supporting Information S1. After a period of quasi-steady-state creep, the load was removed entirely before the next strain cycle. When changing temperature, the sample was allowed to anneal for ∼30 min before a new load was applied. No substantial grain growth was anticipated on the experimental timescales, as grain boundary migration is generally slow in multiphase aggregates. In several experiments, conditions of temperature and differential stress investigated in an early constant-load step were revisited later to test for reproducibility and to identify potential changes in mechanical behavior resulting from microstructural evolution. Measurements of strain rate at constant stress in the initial stages of some experiments did show anomalously high strain rates relative to later tests at similar stresses, suggesting early realignment of the sample and/or adjustment of sample microstructure; in these cases, the data were not used in

the subsequent analysis. The total shortening strains achieved in the different experiments ranged from 3.5% to 19.1%, as delineated in Table 2. Several temperature-stepping experiments were performed at a confining pressure of 300 MPa and differential stresses of ∼225 MPa to determine the activation energy for dislocation creep in the protoenstatite field.

Strain rates and flow stresses were calculated from the displacement and load data, allowing for determination of the instantaneous sample length and cross-sectional area, and correcting the data for the load supported by the nickel jacket and the iron sleeve using Ni and Fe flow laws (Frost & Ashby, 1982).

2.4. Microstructural and Textural Characterization

All available hot-pressed and deformed samples that were suitable for analysis were analyzed by optical microscopy and scanning electron microscopy (SEM) utilizing orientation contrast (OC) and electron backscatter diffraction (EBSD). Petrographic axial thin sections ∼20–30 μm thick were prepared for optical microscopy. SEM measurements were performed either on the planar surface of an axially split sample cylinder or on axial thin sections prepared from the samples after polishing, including with a high-pH colloidal silica suspension for several hours. Starting samples were analyzed at the Université de Toulouse using a JEOL JSM-7100TTLS LV with a Schottky field emission gun (FEG) cathode operating at an accelerating voltage of 20 keV and a beam current of 50 nA at a working distance of 15 mm. Samples were coated with a carbon layer of about 15 nm. Diffraction patterns were recorded with a CMOS Symmetry S2 detector from Oxford Instruments. Deformed microstructures were analyzed at the Bayerisches Geoinstitut of the Universität Bayreuth, Germany, using a Zeiss Gemini 1530 SEM with a Schottky FEG cathode operating at an accelerating voltage of 20 keV and a beam current of about 2 nA at a working distance of 16 mm. Samples were coated with a carbon layer of about 2–3 nm. Diffraction patterns were recorded with a Nordlys II camera from Oxford Instruments. On both systems, diffraction patterns were automatically indexed with the Aztec software using similar settings. High-resolution orientation imaging maps were acquired with a step size of 0.25 or 1 micron and were used to obtain grain size distributions in the samples before and after deformation. Average grain sizes were estimated as the equivalent 2D-diameters of the average grain surfaces in the maps. Diffraction patterns were also recorded with larger step sizes (up to 50 μm) to generate pole figures describing the overall bulk texture of the samples.

3. Experimental Results

3.1. Deformation Results

Deformation experiments were performed on enstatite-olivine samples under conditions where the enstatite was predominantly in either the protoenstatite or the orthoenstatite field. Hot-pressing and deformation conditions are detailed in Tables 1 and 2, respectively. The two tables also contain the average grain sizes for enstatite and olivine in those hot-pressed and deformed samples for which suitable material was available. The pressure and temperature conditions and the creep data derived from each creep test in the protoenstatite and orthoenstatite fields are listed in Tables 3 and 4, respectively. Experiments performed at a confining pressure P_c of 300 MPa (PI-343, PI-399, PI-400, PI-450, PI-453, PI-454, PI-455 and PI-458) were mostly in the protoenstatite field or possibly a mixed protoenstatite and orthoenstatite field, although tests at temperatures below 1244°C technically fall within the orthoenstatite field (see also Figure 1 in Bystricky et al., 2016). As discussed in Section 4.1, the sluggish transformation kinetics may have resulted in retention of the enstatite grains metastably within the protoenstatite field during excursions to lower temperatures. All experiments at P_c = 450 MPa (PI-541, PI-553, PI-560, and PI-561) were entirely in the orthoenstatite field.

Under the experimental conditions of this study, synthetic monocrystalline aggregates composed of enstatite or olivine with grain sizes in the range 5–20 μm deform predominantly by diffusion creep at lower stresses and dislocation creep at higher stresses (e.g., Bystricky et al., 2016; Mei & Kohlstedt, 2000a, 2000b). Some level of mixed-mode deformation was observed, with contributions of both mechanisms under a broad range of conditions at intermediate stresses. As noted below, the diffusion creep component showed a strong dependence on grain size while the dislocation creep component consistently showed none. Thus, while some component of grain-boundary sliding may occur in these samples (e.g., Hirth & Kohlstedt, 2003), the data fit well to a model with only diffusion and dislocation creep components. Assuming that the two components are independent and that the stress exponent for diffusion creep is $n = 1$ (see e.g., Bystricky et al., 2016), the rheology of the enstatite-olivine aggregates can be described empirically by:

Table 3
Creep Data for Enstatite-Olivine Aggregates at a Confining Pressure P_c of 300 MPa

Exp.	Composition (vol.%)	P_c (MPa)	T (°C)	σ (MPa)	$\dot{\varepsilon}$ (s^{-1})	ε (%)
PI-400	75%En-25%Ol	300	1200	169	$9.2 \pm 1.4 \times 10^{-7}$	0.8
				229	$2.0 \pm 0.3 \times 10^{-6}$	0.9
				202	$1.2 \pm 0.1 \times 10^{-6}$	0.6
			1250	170	$3.8 \pm 0.5 \times 10^{-6}$	2.1
				86	$1.2 \pm 0.2 \times 10^{-6}$	0.7
				116	$2.1 \pm 0.3 \times 10^{-6}$	0.6
			1297	85	$5.6 \pm 0.7 \times 10^{-6}$	0.9
				143	$1.1 \pm 0.1 \times 10^{-5}$	0.9
				203	$2.8 \pm 0.4 \times 10^{-5}$	1.0
PI-458	75%En-25%Ol	300	1297	232	$2.5 \pm 0.3 \times 10^{-5}$	2.0
			1271	229	$9.7 \pm 1.2 \times 10^{-6}$	1.4
			1250	228	$4.8 \pm 0.6 \times 10^{-6}$	1.4
			1227	227	$2.2 \pm 0.3 \times 10^{-6}$	1.5
			1200	226	$9.4 \pm 1.8 \times 10^{-7}$	1.1
PI-343	50%En-50%Ol	300	1300	160	$2.3 \pm 0.2 \times 10^{-5}$	1.6
				40	$2.1 \pm 0.5 \times 10^{-6}$	1.0
				61	$3.4 \pm 0.4 \times 10^{-6}$	1.0
				82	$4.9 \pm 0.7 \times 10^{-6}$	1.0
				103	$6.6 \pm 0.8 \times 10^{-6}$	0.9
				124	$1.0 \pm 0.2 \times 10^{-5}$	1.0
				144	$1.2 \pm 0.2 \times 10^{-5}$	1.3
				164	$1.6 \pm 0.1 \times 10^{-5}$	1.2
				184	$2.0 \pm 0.2 \times 10^{-5}$	1.1
				205	$2.7 \pm 0.4 \times 10^{-5}$	1.2
				225	$3.1 \pm 0.4 \times 10^{-5}$	1.2
				241	$4.3 \pm 0.5 \times 10^{-5}$	1.1
				260	$6.0 \pm 0.8 \times 10^{-5}$	1.1
			1244	160	$2.6 \pm 0.3 \times 10^{-6}$	0.9
				173	$2.4 \pm 0.3 \times 10^{-6}$	0.8
				218	$4.3 \pm 0.5 \times 10^{-6}$	0.9
				233	$5.5 \pm 0.7 \times 10^{-6}$	1.0
				251	$7.2 \pm 0.9 \times 10^{-6}$	0.8
PI-450	50%En-50%Ol	300	1304	52	$1.8 \pm 0.4 \times 10^{-6}$	0.9
				82	$2.5 \pm 0.3 \times 10^{-6}$	1.1
				111	$3.7 \pm 0.5 \times 10^{-6}$	1.1
			1279	55	$4.5 \pm 0.6 \times 10^{-7}$	0.7
				85	$8.1 \pm 1.0 \times 10^{-7}$	0.6
				114	$1.3 \pm 0.1 \times 10^{-6}$	0.7
PI-455	50%En-50%Ol	300	1296	222	$3.2 \pm 0.4 \times 10^{-5}$	1.3
			1275	222	$1.7 \pm 0.2 \times 10^{-5}$	1.7
			1250	222	$1.1 \pm 0.1 \times 10^{-5}$	1.8
			1222	224	$6.6 \pm 0.8 \times 10^{-6}$	1.6
			1202	226	$4.6 \pm 0.6 \times 10^{-6}$	1.4
			1175	225	$2.6 \pm 0.4 \times 10^{-6}$	1.5
PI-399	25%En-75%Ol	300	1300	146	$4.9 \pm 0.7 \times 10^{-5}$	1.7

Table 3
Continued

Exp.	Composition (vol.%)	P_c (MPa)	T (°C)	σ (MPa)	$\dot{\varepsilon}$ (s^{-1})	ε (%)
			1200	172	$4.0 \pm 0.5 \times 10^{-6}$	0.9
				97	$1.2 \pm 0.1 \times 10^{-6}$	0.6
				198	$4.8 \pm 0.7 \times 10^{-6}$	0.9
				112	$1.4 \pm 0.1 \times 10^{-6}$	0.7
				229	$6.8 \pm 0.9 \times 10^{-6}$	0.9
				149	$2.3 \pm 0.3 \times 10^{-6}$	0.5
			1251	113	$7.1 \pm 0.9 \times 10^{-6}$	0.9
				55	$2.1 \pm 0.3 \times 10^{-6}$	0.6
				141	$9.8 \pm 1.9 \times 10^{-6}$	0.8
				85	$3.6 \pm 0.5 \times 10^{-6}$	0.6
				170	$1.6 \pm 0.2 \times 10^{-5}$	0.9
			1300	113	$2.1 \pm 0.3 \times 10^{-5}$	1.1
				56	$7.8 \pm 1.2 \times 10^{-6}$	0.6
PI-453	25%En-75%Ol	300	1300	108	$1.7 \pm 0.2 \times 10^{-5}$	1.4
				54	$3.9 \pm 0.5 \times 10^{-6}$	1.1
				82	$6.6 \pm 0.9 \times 10^{-6}$	1.0
PI-454	25%En-75%Ol	300	1197	221	$4.9 \pm 0.8 \times 10^{-6}$	1.2
			1183	223	$2.2 \pm 0.3 \times 10^{-6}$	1.1
			1225	223	$9.9 \pm 1.2 \times 10^{-6}$	1.1
			1245	222	$1.7 \pm 0.2 \times 10^{-5}$	1.4
			1270	222	$3.9 \pm 0.5 \times 10^{-5}$	1.0
			1300	222	$1.1 \pm 0.1 \times 10^{-4}$	0.7

$$\dot{\varepsilon} = \dot{\varepsilon}_{\text{diff}} + \dot{\varepsilon}_{\text{disl}} = \text{A}_{\text{diff}} \frac{\sigma}{d^m} \exp\left(-\frac{Q_{\text{diff}}}{\text{R}T}\right) + \text{A}_{\text{disl}}\, \sigma^n \exp\left(-\frac{Q_{\text{disl}}}{\text{R}T}\right) \quad (1)$$

where $\dot{\varepsilon}$ is the total strain rate, $\sigma = \sigma_1 - \sigma_3$ is the differential stress, d is grain size, T is temperature, R is the gas constant, and A_{diff}, m, Q_{diff}, A_{disl}, n and Q_{disl} are empirical parameters characterizing the diffusion creep and the dislocation creep components $\dot{\varepsilon}_{\text{diff}}$ and $\dot{\varepsilon}_{\text{disl}}$ (e.g., Poirier, 1985). On the assumption that the diffusion creep component is rate-limited by grain-boundary diffusion (Coble creep), we fixed the value of the grain-size exponent as $m = 3$, as in prior studies by Bystricky and Mackwell (2001) on clinopyroxene, Bystricky et al. (2016) on enstatite, and Hirth and Kohlstedt (1995a) on olivine aggregates. It should be noted that while the flow law for the dislocation creep component (and similarly, diffusion creep component) for a polyphase aggregate is more complex than a simple power law, a power law can provide a good first-order approximation (Tullis et al., 1991; see also Sections 4.3 and 4.4 in discussion below).

High-resolution SEM-EBSD maps acquired for all suitable hot-pressed and deformed samples (shown in Figures S2 and S3 in Supporting Information S1) allowed the determination of grain size distributions (Figures S4 and S5 in Supporting Information S1) and estimates of average grain sizes (Tables 1 and 2). As can be seen from the data in Table 1, grain size after hot-pressing for both enstatite and olivine generally increases with duration of the hot press. This is most notable for the olivine grains, which have average grain sizes around ~7 μm after 4–5 hr and ~13 μm after 8 hr. By contrast, comparison of the grain sizes after hot-pressing with those for the same sample after deformation shows only very minor grain growth subsequent to the hot-pressing stage (e.g., PI-343 and PI-453, Tables 1 and 2), providing some confidence that grain growth during deformation was limited. In fitting the deformation flow law to the data from each experiment using Equation 1, we used estimates based on the grain-size measurements for hot-pressed or deformed samples shown in Tables 1 and 2. While we do not have measurements for all samples, there is some consistency in the data. We estimated grain sizes of ~7 μm for both

Table 4
Creep Data for Enstatite-Olivine Aggregates at a Confining Pressure P_c of 450 MPa

Exp.	Composition (vol.%)	P_c (MPa)	T (°C)	σ (MPa)	$\dot{\varepsilon}$ (s^{-1})	ε (%)
PI-560	75%En-25%Ol	450	1199	279	$1.6 \pm 0.2 \times 10^{-5}$	1.3
				347	$2.4 \pm 0.3 \times 10^{-5}$	1.0
				404	$3.8 \pm 0.5 \times 10^{-5}$	1.0
			1150	292	$3.6 \pm 0.4 \times 10^{-6}$	1.0
				350	$4.8 \pm 0.6 \times 10^{-6}$	1.1
				406	$7.4 \pm 0.9 \times 10^{-6}$	1.0
			1175	282	$6.1 \pm 0.8 \times 10^{-6}$	1.0
				340	$8.5 \pm 1.1 \times 10^{-6}$	1.0
				397	$1.5 \pm 0.2 \times 10^{-5}$	1.0
			1199	358	$2.3 \pm 0.4 \times 10^{-5}$	1.1
			1225	298	$2.8 \pm 0.4 \times 10^{-5}$	1.0
				358	$4.6 \pm 0.5 \times 10^{-5}$	1.2
				421	$7.6 \pm 0.9 \times 10^{-5}$	1.6
			1250	299	$6.0 \pm 0.7 \times 10^{-5}$	1.3
PI-561	50%En-50%Ol	450	1150	396	$1.7 \pm 0.3 \times 10^{-5}$	0.9
			1175	280	$1.1 \pm 0.1 \times 10^{-5}$	1.0
				338	$1.6 \pm 0.3 \times 10^{-5}$	1.1
				395	$2.6 \pm 0.4 \times 10^{-5}$	1.3
			1200	282	$1.9 \pm 0.3 \times 10^{-5}$	1.1
				338	$3.5 \pm 0.5 \times 10^{-5}$	1.2
PI-541	40%En-60%Ol	450	1250	110	$1.6 \pm 0.4 \times 10^{-5}$	1.1
				54	$6.1 \pm 1.2 \times 10^{-6}$	1.2
				83	$9.9 \pm 1.7 \times 10^{-6}$	1.0
				140	$1.8 \pm 0.3 \times 10^{-5}$	1.1
				167	$2.4 \pm 0.5 \times 10^{-5}$	1.0
				195	$3.0 \pm 0.6 \times 10^{-5}$	1.4
				224	$4.2 \pm 0.7 \times 10^{-5}$	1.6
			1200	112	$2.8 \pm 0.6 \times 10^{-6}$	1.1
				167	$4.8 \pm 0.9 \times 10^{-6}$	1.2
				225	$8.4 \pm 1.7 \times 10^{-6}$	1.1
				285	$1.5 \pm 0.3 \times 10^{-5}$	1.6
				343	$2.6 \pm 0.4 \times 10^{-5}$	1.0
				401	$4.1 \pm 0.9 \times 10^{-5}$	1.5
				198	$6.4 \pm 1.3 \times 10^{-6}$	1.3
			1250	170	$2.2 \pm 0.3 \times 10^{-5}$	1.4
PI-553	25%En-75%Ol	450	1250	49	$2.0 \pm 0.3 \times 10^{-6}$	1.0
				142	$9.9 \pm 1.3 \times 10^{-6}$	1.0
				115	$5.9 \pm 0.8 \times 10^{-6}$	1.1
				86	$3.4 \pm 0.4 \times 10^{-6}$	1.1
			1225	171	$5.7 \pm 0.7 \times 10^{-6}$	1.0
				117	$2.4 \pm 0.4 \times 10^{-6}$	1.1
				145	$3.6 \pm 0.5 \times 10^{-6}$	1.1

Table 5
Stress Exponents for the Dislocation Creep Component From NLS Regression Fits to the Creep Data for Samples Deformed at a Confining Pressure of 300 (Protoenstatite) and 450 MPa (Orthoenstatite)

Exp.	Composition (vol%)	n
PROTOENSTATITE		
PI-339	100%En	3.2 ± 0.6
PI-402	100%En	4.9 ± 2.9
PI-400	75%En-25%Ol	4.4 ± 1.0
PI-458[a]	75%En-25%Ol	–
PI-343	50%En-50%Ol	3.4 ± 0.5
PI-450	50%En-50%Ol	–
PI-455[a]	50%En-50%Ol	–
PI-399	25%En-75%Ol	3.7 ± 0.7
PI-453	25%En-75%Ol	–
PI-454[a]	25%En-75%Ol	–
Protoenstatite Mean[b]:		3.5 ± 0.3
ORTHOENSTATITE		
PI-512	100%En	3.2 ± 0.6
PI-539	100%En	3.5 ± 0.3
PI-560	75%En-25%Ol	6.5 ± 2.9
PI-561	50%En-50%Ol	2.9 ± 0.4
PI-541	40%En-60%Ol	4.1 ± 0.4
PI-553	25%En-75%Ol	6.2 ± 1.5
Orthoenstatite Mean[b]:		3.5 ± 0.2
Mean[b] of All:		3.5 ± 0.2

Note. All uncertainties are 1σ. [a]Temperature-stepping experiments at a constant stress. [b]Uncertainties in n were propagated in the calculations of the mean values.

enstatite and olivine in samples initially hot-pressed for 2–6 hr, and ~8 μm for enstatite grains and ~14 μm for olivine grains in samples hot-pressed for 8 hr.

Fitting the complete flow law (Equation 1), encompassing both diffusion and dislocation creep components with 5 free parameters (log A_{diff}, Q_{diff}, log A_{disl}, n, and Q_{disl}), to data from a given experiment requires application of a non-linear least squares (NLS) regression. For a subset of the experiments (PI-402, PI-450, PI-453 and PI-561), we had to fix values for the stress exponent n and/or the activation energy Q_{disl} for the dislocation creep component to converge on a unique solution. For all other experiments, the range of conditions (T, σ, $\dot{\varepsilon}$) in each creep field was sufficient to fit Equation 1 to the data and determine all free parameters (the stress exponents n are listed in Table 5). A weighted mean of the stress exponent values, with each data point weighted according to its uncertainty (as described in Text S1 in Supporting Information S1 and illustrated in Figure S6 in Supporting Information S1), yielded an average stress exponent of $n = 3.5 \pm 0.3$ for samples deformed in the protoenstatite field and $n = 3.5 \pm 0.2$ for those in the orthoenstatite field (Table 5). It should be noted that these values are similar to the stress exponents for dislocation creep determined in previous studies for olivine (e.g., $n = 3.5 \pm 0.3$, Hirth & Kohlstedt, 2003) and enstatite aggregates (e.g., $n \sim 3$, Bystricky et al., 2016). Based on the consistency of these results, we fixed $n = 3.5$ and performed new NLS regressions for data from each experiment to determine the other parameters (log A_{diff}, Q_{diff}, log A_{disl}, and Q_{disl}), which are quoted in Tables 6 and 7.

3.1.1. Protoenstatite Experiments

Data from experiments in the protoenstatite stability field are listed in Table 3 and flow law parameters determined by NLS fits are in Table 6. Both the data and the fits are plotted in Figure 1. Two experiments on aggregates containing 100% enstatite (PI-339 and PI-402, Figure 1a), previously reported by Bystricky et al. (2016), were reanalyzed with the same procedure as all the other experiments to ensure a consistent approach to the data analysis. The activation energy for dislocation creep for PI-339 of $Q_{disl} = 652 \pm 110$ kJ/mol obtained using this fitting method is in good agreement with the value of

Table 6
Deformation Parameters From NLS Regression Fits to the Creep Data Using n = 3.5 for the Dislocation Creep Component for Samples Deformed at a Confining Pressure of 300 MPa Predominantly in the Protoenstatite Field

Exp.	Composition (vol%)	log(A_{disl})[a]	Q_{disl} (kJ/mol)	log(A_{diff})[b]	Q_{diff} (kJ/mol)
PI-339	100%En	8.5 ± 3.7	652 ± 110	24.4 ± 7.2	884 ± 215
PI-402	100%En	8.9 ± 0.1	652[d]	24.7 ± 0.1	884[d]
PI-400	75%En-25%Ol	4.9 ± 1.7	537 ± 49	16.9 ± 1.8	648 ± 54
PI-458[c]	75%En-25%Ol	16.9 ± 0.6	648 ± 17	–	–
PI-343	50%En-50%Ol	11.5 ± 3.1	732 ± 93	16.5 ± 3.7	640 ± 110
PI-450	50%En-50%Ol	10.9 ± 0.2	732[d]	29.8 ± 2.3	1046 ± 70
PI-455[c]	50%En-50%Ol	16.3	624	–	–
PI-399	25%En-75%Ol	8.9 ± 1.5	632 ± 42	11.6 ± 1.2	482 ± 34
PI-453	25%En-75%Ol	8.9 ± 0.1	632[d]	12.2 ± 0.1	482[d]
PI-454[c]	25%En-75%Ol	16.1 ± 0.9	605 ± 27	–	–

Note. All uncertainties are 1σ. [a]A_{disl} is in units of $MPa^{-n}s^{-1}$. [b]A_{diff} is in units of MPa^{-1} μm^3 s^{-1}. [c]Temperature-stepping experiments at a constant stress. [d]Activation energies used in the NLS regression fits were fixed at values for the other sample of the same composition as there were insufficient data to fully constrain the fitting routines.

Table 7
Deformation Parameters From NLS Regression Fits to the Creep Data Using n = 3.5 for the Dislocation Creep Component for Samples Deformed at a Confining Pressure of 450 MPa in the Orthoenstatite Field

Exp.	Composition (vol%)	$\log(A_{disl})$[a]	Q_{disl} (kJ/mol)	$\log(A_{diff})$[b]	Q_{diff} (kJ/mol)
PI-512	100%En	5.8 ± 1.9	561 ± 55	16.3 ± 1.9	613 ± 55
PI-539	100%En	7.1 ± 1.5	594 ± 54	14.4 ± 3.9	568 ± 115
PI-560	75%En-25%Ol	6.0 ± 3.6	556 ± 102	11.7 ± 5.0	468 ± 139
PI-561[c]	50%En-50%Ol	2.8 ± 1.9	454 ± 54	–	–
PI-541	40%En-60%Ol	2.0 ± 2.8	439 ± 79	18.1 ± 1.1	651 ± 30
PI-553	25%En-75%Ol	9.4 ± 10.1	651 ± 294	23.3 ± 8.5	796 ± 247

Note. All uncertainties are 1σ. [a]A_{disl} is in units of $MPa^{-n}s^{-1}$. [b]A_{diff} is in units of MPa^{-1} μm^3 s^{-1}. [c]There were insufficient data at low stresses to constrain the diffusion creep component.

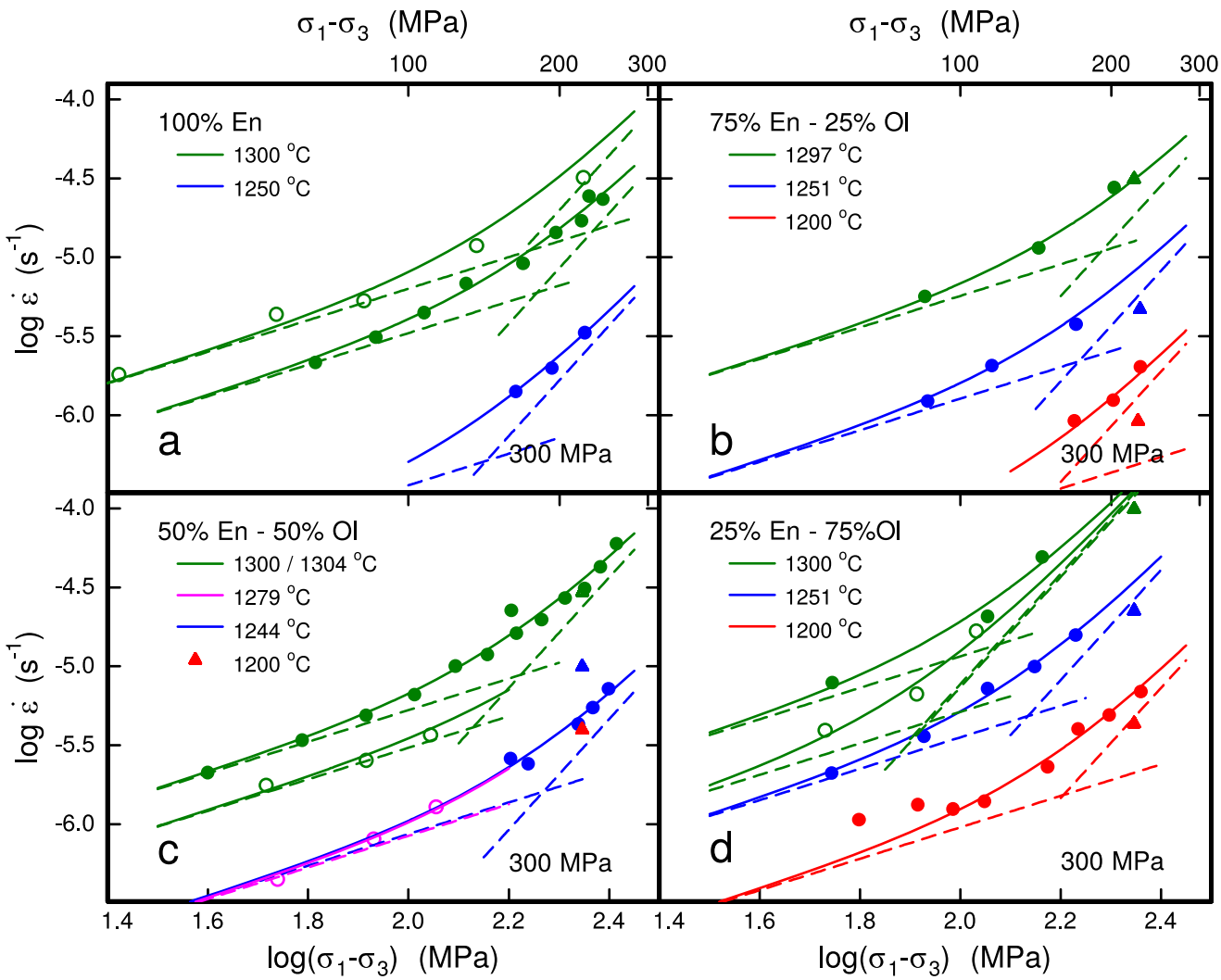

Figure 1. Deformation results under conditions where enstatite was mostly in the protoenstatite stability field for samples containing (a) 100 vol% enstatite, showing data from experiments PI-339 (solid circles) and PI-402 (hollow circles) - creep data from Bystricky et al. (2016) with fits to the data recalculated for this study; (b) 75 vol% enstatite and 25 vol% olivine, showing data from experiments PI-400 (solid circles) and PI-458 (triangles); (c) 50 vol% enstatite and 50 vol% olivine, showing data from experiments PI-343 (solid circles), PI-450 (hollow circles), and PI-455 (triangles); and (d) 25 vol% enstatite and 75 vol% olivine, showing data from experiments PI-399 (solid circles), PI-453 (hollow circles), and PI-454 (triangles). The solid lines show NLS regression fits to the data for each experiment. The dashed lines show the components of the fits for diffusion and dislocation creep.

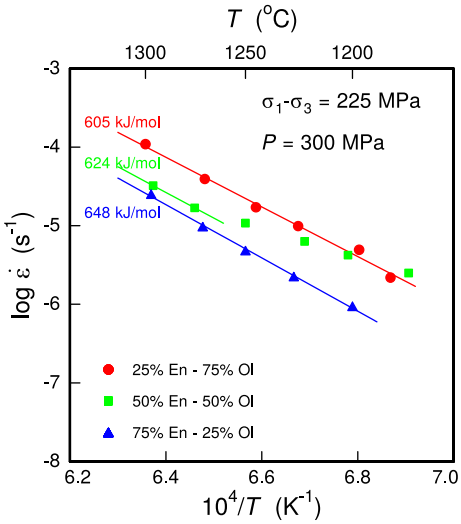

Figure 2. Deformation results for samples PI-454 (red), PI-455 (green) and PI-458 (blue) mostly within the protoenstatite stability field. These experiments were conducted over a variety of temperatures at a constant stress of ~225 MPa. The quoted activation energies for creep were determined from least squares regression fits to the data for each experiment. In the case of PI-455, the activation energy was calculated only for the two highest temperatures since diffusion creep seems to contribute increasingly at lower temperatures.

~720 kJ/mol reported by Bystricky et al. (2016) for this experiment. Since the experimental data from PI-402 did not explore far into the dislocation creep realm and only a single temperature was investigated, we fixed $n = 3.5$, $Q_{disl} = 652$ kJ/mol and $Q_{diff} = 884$ kJ/mol in the NLS fit to the data, assuming the same activation energies as those determined for PI-339.

The creep data from two experiments performed on aggregates containing 75 vol% enstatite and 25 vol% olivine (PI-400 and PI-458) are shown in Figure 1b. For PI-458, only data at similar temperatures to those for PI-400 are shown; they are consistent with the fitted curves for dislocation creep (dashed lines) from that experiment. The full data set for PI-458, which was deformed over a range of temperatures at a constant stress, is shown in Figure 2.

Flow law fits to the creep data from two experiments performed on aggregates containing 50 vol% enstatite and 50 vol% olivine (PI-343 and PI-450) are shown in Figure 1c. Since the experimental data from PI-450 did not explore far into the dislocation creep realm, we used $n = 3.5$ and $Q_{disl} = 732$ kJ/mol (as calculated for PI-343) in the NLS fit. Although PI-455 was deformed at a differential stress of ~225 MPa for a range of temperatures, it appears to show increasing strain rate contributions due to diffusion creep at temperatures below 1275°C (Figure 2) and consequently these data were not included in the dislocation creep analysis. These observations are consistent with diffusion creep predominance in PI-450, an earlier deformation experiment on the same sample.

Creep data from the three experiments (PI-399, PI-453 and PI-454) performed on aggregates containing 25 vol% enstatite and 75 vol% olivine in the protoenstatite field are plotted in Figures 1d and 2. Since only a single temperature was investigated for PI-453, we fixed $Q_{disl} = 632$ kJ/mol and $Q_{diff} = 482$ kJ/mol in the NLS fit to the data, assuming the same activation energies as for PI-399. While there are clear differences in creep rates at each stress between experiments in the diffusion creep realm, likely due to grain size differences, the dislocation creep data show good consistency.

3.1.2. Orthoenstatite Experiments

Data and fitted flow law parameters for experiments in the orthoenstatite stability field are listed in Tables 3 and 7, respectively, and plotted in Figure 3. Experiments on pure orthoenstatite samples (PI-512 and PI-539, Figure 3a), previously reported by Bystricky et al. (2016), were reanalyzed using the same procedure as for the other experiments for consistency. Fits of Equation 1 to the data for each experiment yield activation energies for dislocation creep of $Q_{disl} = 561 \pm 55$ kJ/mol (PI-512) and $Q_{disl} = 594 \pm 54$ kJ/mol (PI-539), in excellent agreement with the value of 600 ± 21 kJ/mol reported previously (Bystricky et al., 2016). Fitting the combined data from PI-512 and PI-539 after subtracting the diffusion creep component, we obtain the following flow law for orthoenstatite aggregates deforming in the dislocation creep field:

$$\dot{\varepsilon}_{disl} = 10^{6.4\pm0.7}\,\sigma^{3.5}\exp\left(-\frac{577 \pm 19\ \text{kJ/mol}}{RT}\right) \quad (2)$$

where $\dot{\varepsilon}_{disl}$ is the dislocation creep rate, $\sigma = \sigma_1 - \sigma_3$ is the differential stress in MPa, T is temperature in K, R is the gas constant, and the flow law parameters are $n = 3.5$, $Q_{disl} = 577 \pm 19$ kJ/mol and $A_{disl} = 10^{6.4\pm0.7}$ MPa$^{-3.5}$s^{-1} (Figure 4).

The creep data from PI-560, which was performed on an aggregate containing 75 vol% enstatite and 25 vol% olivine, are shown in Figure 3b. The experiment performed on an aggregate containing 50 vol% enstatite and 50 vol% olivine (PI-561, Figure 3c) only yielded parameters for the dislocation creep component in Equation 1 since the limited range of differential stresses tested in this experiment made it impossible to provide constraints on the diffusion creep component. Creep data from experiments on an aggregate containing 40 vol% enstatite and 60

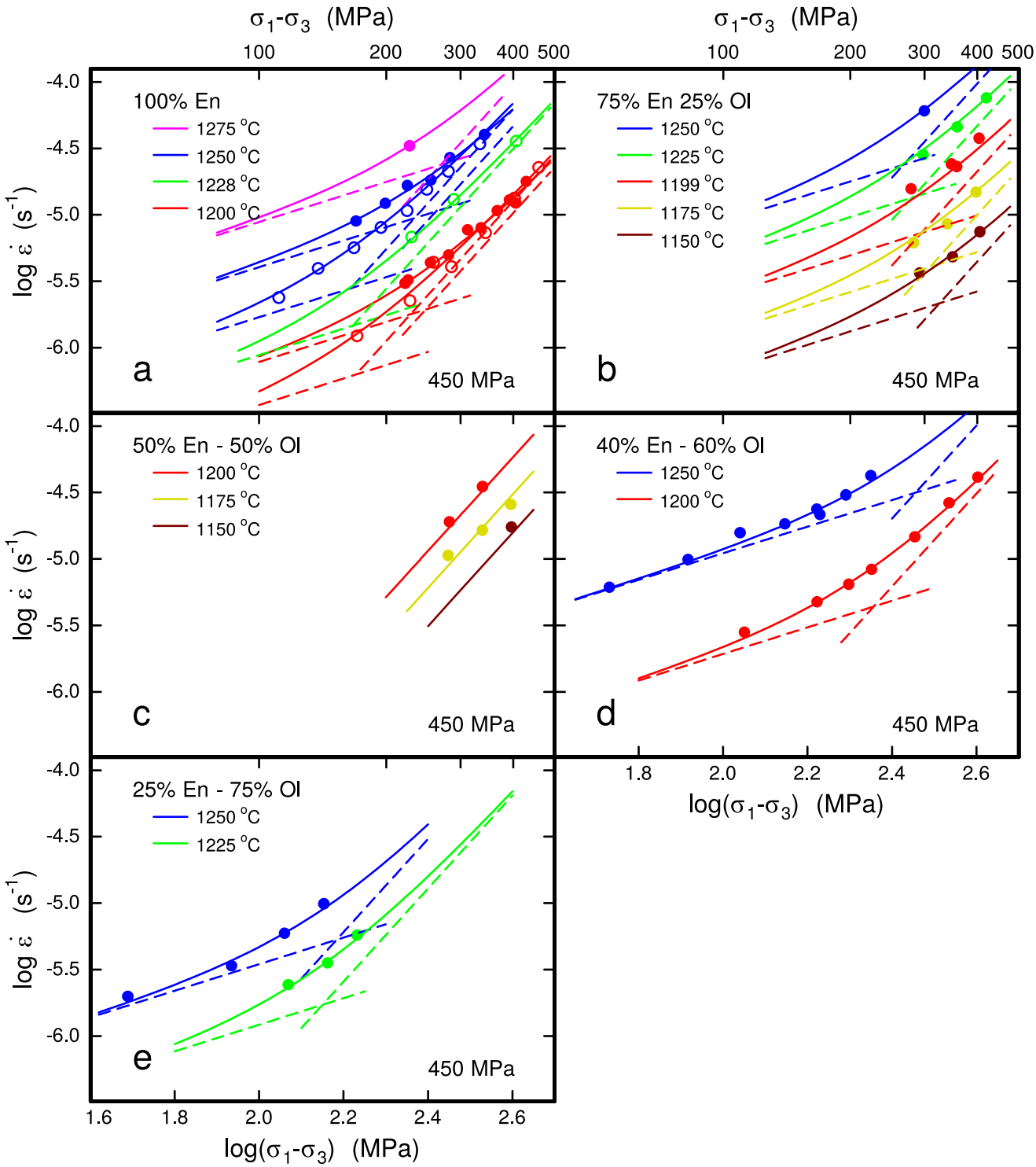

Figure 3. Deformation results under conditions where enstatite was in the orthoenstatite stability field for samples containing (a) 100 vol% enstatite, showing data from experiments PI-512 (solid circles) and PI-539 (hollow circles) - creep data from Bystricky et al. (2016) with fits to the data recalculated for this study; (b) 75 vol% enstatite and 25 vol% olivine, showing data from experiment PI-560; (c) 50 vol% enstatite and 50 vol% olivine, showing data from experiment PI-561; (d) 40 vol% enstatite and 60 vol% olivine, showing data from experiment PI-541; and (e) 25 vol% enstatite and 75 vol% olivine, showing data from experiment PI-553. The solid lines show the NLS regression fits to the data. The dashed lines show the components of the fits for diffusion and dislocation creep.

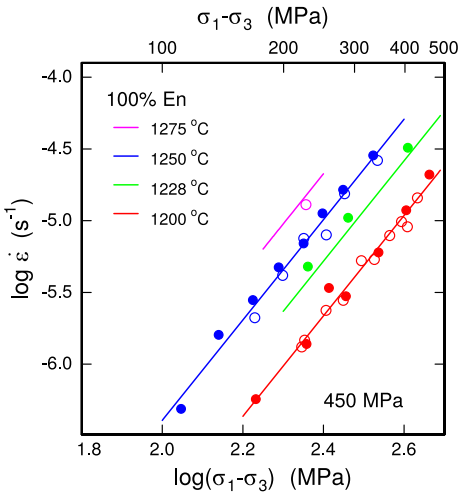

Figure 4. Deformation results under conditions where enstatite was in the orthoenstatite stability field for samples containing 100 vol% enstatite, showing data from experiments PI-512 (hollow circles) and PI-539 (solid circles)—creep data from Bystricky et al. (2016). The diffusion creep component was subtracted from the data using the NLS fits for each experiment. The resulting data for the two experiments were fit to a dislocation flow law using a linear least squares regression, which yielded $Q_{disl} = 577 \pm 19$ kJ/mol and $\log A_{disl} = 6.4 \pm 0.7$ for an assumed value of $n = 3.5$.

vol% olivine (PI-541) and on an aggregate containing 25 vol% enstatite and 75 vol% olivine (PI-553), are shown in Figures 3d and 3e, respectively.

3.2. Microstructures and Textures

As noted by Bystricky et al. (2016), quenching of samples after deformation in the protoenstatite field results in transformation of the enstatite grains mostly to low clinoenstatite (e.g., Huebner, 1980), the stable form of enstatite at low temperature and pressure. For enstatite grains deformed in the orthoenstatite field, both the high stresses imposed during deformation and high quenching rates favor the formation of clinoenstatite lamellae within orthoenstatite grains (e.g., Buseck et al., 1980; Coe & Kirby, 1975). In both cases, these transformations significantly overprint deformation microstructures in the enstatite phase. In the EBSD analysis we used the clinoenstatite structure for indexing the enstatite patterns since it yielded a more robust solution. The twin lamellae that were resolved with the clinoenstatite structure are defined by a 180° rotation around the [001] axis and were ignored in the following grain size analysis. In addition, microfracturing at grain boundaries, which resulted from local stress concentrations due to phase transformation and thermal stresses during quenching under load, caused some grain plucking during sample preparation for SEM and EBSD measurements.

3.2.1. Deformation Microstructures

Starting microstructures show well-mixed aggregates with near-equant grain shapes (Figure S2 in Supporting Information S1). Four samples with varying amounts of the two phases deformed in the protoenstatite field (PI-343, PI-399, PI-400, PI-453) were investigated with SEM-EBSD techniques to characterize their deformation microstructure and texture (crystallographic preferred orientations, CPO). Both microstructures and textures are rather similar independent of phase proportions and thus results are displayed here for one representative sample (PI-399, 75 vol% olivine, 25 vol% enstatite). Figure 5 shows an orientation contrast image (OC) taken with a forescatter detector next to an EBSD map of the same area displaying the phase information and grain and phase boundaries. The grain structure of both phases is rather homogeneous and does not show any indications of strain localization. Grain shapes for both phases are equant to slightly elongated perpendicular to the compression direction. Olivine and enstatite grains in the OC images show indications of subgrain boundaries and incipient recrystallization is observed in some larger olivine and enstatite grains. All other EBSD maps acquired on deformed samples are shown in Figure S3 in Supporting Information S1.

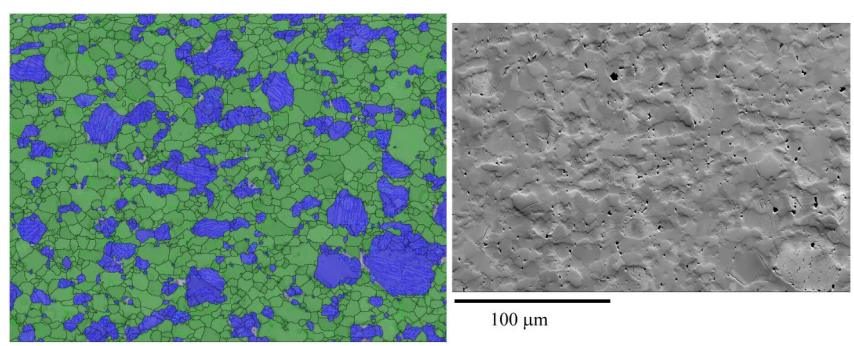

Figure 5. Microstructure of deformed sample PI-399 (75 vol% olivine, 25 vol% enstatite); compression direction is vertical. Left: SEM-EBSD map with olivine and enstatite grains marked in green and blue, respectively; black lines are large angle ($\omega > 10°$) grain boundaries and phase boundaries; light green and light blue lines are subgrain boundaries ($\omega > 1°$) for olivine and enstatite, respectively; dark blue lines are clinoenstatite twins defined by [001] 180° rotations; they were ignored for the grain size analysis. Right: orientation contrast image of the same area.

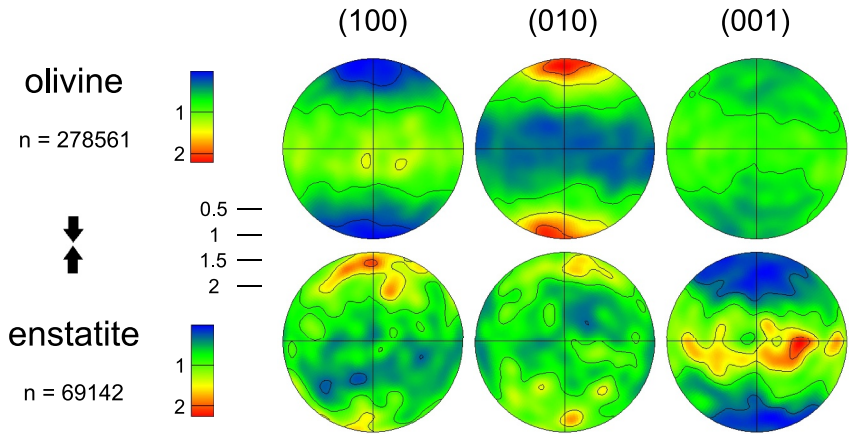

Figure 6. Pole figures of sample PI-399 (75 vol% olivine, 25 vol% enstatite) for olivine (top) and enstatite (bottom); compression direction is vertical; discrete point distributions were smoothed with a Gaussian of 15° in full width half maximum. The contour lines are drawn for multiples of uniform distribution (mud) equal to 0.5, 1, 1.5, and 2. The linear color scales indicate the low intensities in blue and high intensities in red. n indicates the number of measurements; lower-hemisphere, equal area projection.

3.2.2. Crystallographic Preferred Orientations (CPO)

In most of the two-phase hot-pressed samples that were analyzed, the CPOs of both phases are very weak or close to random (see Figure S7 in Supporting Information S1). One exception is sample PI-541, where a weak axisymmetric texture observed in both olivine and enstatite can be explained by compaction during hot-pressing (e.g., Bystricky et al., 2006). In all investigated deformed samples, the CPOs of both phases are more pronounced. They are all quite similar and are represented here by one sample (PI-399, Figure 6; other CPOs are displayed in Figure S8 in Supporting Information S1). In olivine the (010) poles are aligned parallel to the compression direction whereas the [100] and [001] directions lie in girdles perpendicular to the compression direction. For enstatite both (100) and (010) poles are parallel to the compression direction while the [001] directions form a girdle perpendicular to it. Overall texture strengths are not very high (maxima at about 2.2–2.3 m.r.d.), but texture patterns are very clear and smooth. Both phases display axisymmetric orientation distributions reflecting the imposed deformation geometry. The low strength of the CPO is consistent with the low strains and the absence of pervasive recrystallization. The olivine CPOs are consistent with a- and c-slip on the b-planes, whereas the enstatite CPOs indicate c-slip on the a- and b-plane.

4. Discussion

4.1. Deformation Mechanisms

As discussed in Section 3.1 and in Bystricky et al. (2016), enstatite remained in the orthoenstatite field throughout the experiments performed at a confining pressure of 450 MPa. In experiments performed at 300 MPa confining pressure the enstatite grains were mostly in the protoenstatite or mixed protoenstatite-orthoenstatite field, although they would notionally fall within the orthoenstatite field below 1244°C. As can be seen from the experimental data in Figure 1 and Table 3, there is no evidence for significant weakening of samples at the lower temperatures in experiments that straddled both fields, as would be expected if the protoenstatite grains had transformed into orthoenstatite (Bystricky et al., 2016). In addition, in experiments where higher temperatures were revisited after measurements at lower temperatures, the sample behavior replicated that of the earlier measurements. These observations suggest that sluggish kinetics of the transformation from protoenstatite to orthoenstatite may have resulted in metastable retention of protoenstatite.

All deformation experiments show components of diffusion and dislocation creep at lower and higher stresses, respectively (Figures 1 and 3). This is not surprising given the average grain sizes of enstatite (5.6–11.9 μm) and olivine (6.6–14.3 μm) in the hot-pressed samples (Table 1). While there was evidence of coarser grain sizes for each mineral after longer duration of the hot press, a comparison of sample microstructures before

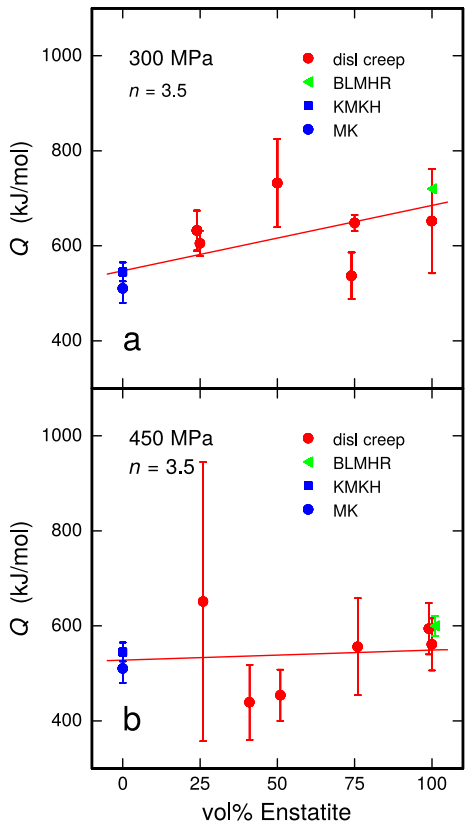

Figure 7. Activation energies for dislocation creep of enstatite-olivine aggregates in (a) the protoenstatite field and (b) the orthoenstatite field, assuming $n = 3.5$ for dislocation creep (Tables 6 and 7). The solid lines show weighted least squares fits to the data including those calculated from the flow laws of Keefner et al. (2011) (KMKH) and Mei and Kohlstedt (2000b) (MK) for olivine aggregates buffered at Ni/NiO, but not the results from Bystricky et al. (2016) for enstatite aggregates (BLMHR) since our results for 100% enstatite were recalculated using their data. Error bars are 1σ.

and after deformation at 300 MPa shows little grain growth during deformation (see Tables 1 and 2, Figures S2 and S3 in Supporting Information S1). Thus, grain size changes were probably also minimal during deformation at 450 MPa. A possible explanation is that grain growth may have been enhanced during the hot-pressing stage by the presence of trapped hydrous species in the cold-pressed powders, while it was likely limited during deformation under very dry conditions. In addition, the systematics of the diffusion creep processes are less well defined and calculated activation energies show significant scatter (Tables 6 and 7). This may be due, in part, to the strong dependence of creep rate in diffusion creep on grain size, which results in a great influence of the grain size distribution on creep rate. Thus, the mere use of average grain size is not appropriate in determining reliable diffusion creep flow laws (Ter Heege et al., 2004; Wang, 1994). Given the distribution of grain sizes in these samples and the complex nature of grain-boundary diffusion creep in two-phase systems, significantly greater microstructural analysis would be required to truly constrain the diffusion creep flow laws. As this study is mostly focused on dislocation creep of the enstatite-olivine two-phase system, we do not report flow laws for diffusion creep and do not analyze the mixing relationships for diffusion creep in enstatite-olivine aggregates.

Numerous previous studies of dislocation creep processes in olivine aggregates have demonstrated the predominance of the (010)[100] slip system, with lesser slip on (001)[100] and (010)[001], at these pressure and temperature conditions (e.g., Durham & Goetze, 1977; Bai et al., 1991; Bai & Kohlstedt, 1992; Keefner et al., 2011; and references therein). Although they are not very strong, the CPOs of olivine grains in our samples are consistent with activation of the (010)[100] and (010)[001] slip systems during deformation. For enstatite, the CPOs are similar to those measured in pure enstatite aggregates deformed under the same conditions (Bystricky et al., 2016). They are indicative of slip on the (100)[001] and (010)[001] slip systems, consistent with TEM observations in previous experimental and natural studies (e.g., Ross & Nielsen, 1978; Van Duysen et al., 1985) and with single crystal experiments (Mackwell, 1991; Raterron et al., 2016).

4.2. Dislocation Creep Flow Laws

As mentioned above and readily seen in Figures 1 and 3, both diffusion and dislocation creep processes are operative over most of the experimental conditions. The relative contribution of dislocation creep to the total strain rate typically varies from ~10% at very low stresses to ~80% or more at high stresses, as illustrated in Figure S9 in Supporting Information S1. Thus, even at the highest stresses, the experimental data are somewhat weaker than the dislocation creep laws derived from the non-linear least squares regression (NLS) fits to the full data set for each experiment (Equation 1). Simple least squares regression fits to just the highest stress data would have underestimated the stress exponents and underestimated the flow stresses for the dislocation creep component, validating the use of NLS regressions to the full data set. Therefore, using this approach and all things otherwise being equal, the dislocation creep laws for samples with the same mixture of phases should be approximately the same, even if the overall measured creep rates differ due to the greater or lesser contributions due to diffusion creep, as can be seen particularly in Figures 1d and 3a.

The use of NLS regression fits to the data for each experiment was not always possible due to the limited number of data points, the need to fit 5 independent parameters (n, log A_{diff}, Q_{diff}, log A_{disl}, Q_{disl}, in Equation 1), and the inherent uncertainties in each data point, as is noted in Tables 6 and 7. While we initially allowed the stress exponent n for dislocation creep to vary, it was clear that a value of $n = 3.5$ was appropriate for all the compositions in both the orthoenstatite and protoenstatite fields (Table 5). This value for n is also very consistent with prior work on single-phase aggregates of olivine (e.g., $n = 3.5 \pm 0.3$, Hirth & Kohlstedt, 2003, and references

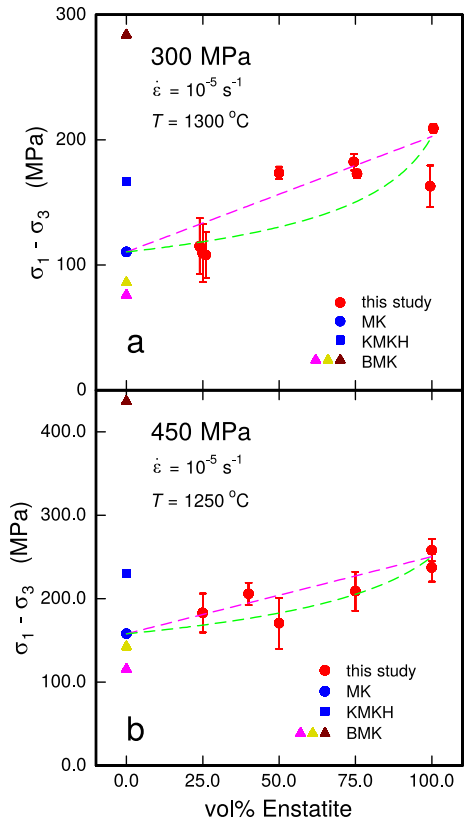

Figure 8. Flow stress versus vol% enstatite at a strain rate of 10^{-5} s^{-1} in enstatite-olivine aggregates deformed in (a) at 1300°C in the protoenstatite field and (b) at 1250°C in the orthoenstatite field. The filled blue circle and square represent calculations using the flow laws for olivine aggregates buffered at Ni/NiO from Mei and Kohlstedt (2000b) (MK) and Keefner et al. (2011) (KMKH), respectively. The triangles show the olivine single-crystal data from Bai et al. (1991) (BMK) for orientations favorable for slip on the slip systems (010)[100] (purple), (001)[100] and (100)[001] (green) and (010)[001] (brown). The error bars represent 1σ bounds based on the NLS regression fits to the experimental data for each experiment. The dashed purple and green lines represent the uniform strain rate (Taylor) and uniform stress (Sachs) bounds, respectively.

therein) and enstatite ($n \sim 3$, Bystricky et al., 2016), and on oriented single crystals of olivine (e.g., $n = 3.5 \pm 0.1$ for all slip systems, Bai et al., 1991) and enstatite ($n = 3.8 \pm 0.5$ for the (100)[001] slip system in protoenstatite, Mackwell, 1991; $n = 3.5 \pm 0.7$ and $n = 4.1 \pm 1.5$ for the (100)[001] and (010)[001] slip systems in orthoenstatite, Raterron et al., 2016).

Under the assumption of $n = 3.5$, NLS regressions to the data for each experiment provided activation energies for dislocation creep of the different two-phase mixtures of enstatite and olivine (Tables 6 and 7). These activation energies were plotted as a function of volume fraction of enstatite in the protoenstatite and orthoenstatite fields (Figures 7a and 7b, respectively), along with the activation energies for dislocation creep for deformation of natural dunite (Keefner et al., 2011), synthetic olivine (Mei & Kohlstedt, 2000b) and synthetic enstatite (Bystricky et al., 2016) under equivalent conditions of temperature, pressure, and oxygen fugacity. The apparent activation energy for creep slightly increases as a function of enstatite content in both fields, although that increase is within the uncertainty of the data, especially for the samples deformed in the orthoenstatite field.

4.3. Effect of Phase Proportions on the Strength of Enstatite-Olivine Aggregates

The goal of the present study, characterizing the effect of phase proportions on polyphase aggregate strength, was to some extent motivated by prior work (Hitchings et al., 1989) that suggested weaker behavior for mixed-phase aggregates than for single-phase aggregates with end-member compositions of enstatite and olivine. A meaningful comparison with other studies requires data sets that have been obtained on similar samples (dry synthetic polycrystalline aggregates) and under similar conditions. In addition, all fine-grained polycrystalline aggregates deform with a component of diffusion creep at lower stresses and/or finer grain sizes (olivine: Hirth & Kohlstedt, 1995b, Mei & Kohlstedt, 2000b; enstatite: Bystricky et al., 2016; enstatite-olivine: this study), which complicates comparisons. For the olivine end-member composition, we selected dislocation creep data for polycrystalline olivine deformed dry under similar conditions and in the same apparatus at the University of Minnesota (Mei & Kohlstedt, 2000b, 1250°C under dry conditions in their Figure 3; for comparisons at 1300°C we extrapolated their results using the activation energy $Q = 510$ kJ/mol given in their Figure 5). For the enstatite end-member, we used a flow stress that was the weighted mean of those calculated using the flow laws for the pure enstatite experiments, allowing for propagation of the errors in those calculations.

Figure 8 shows the strength of enstatite-olivine aggregates in the dislocation creep field as a function of volume fraction of enstatite at conditions reached in most of our experiments in the protoenstatite ($10^{-5}s^{-1}$ and 1300°C, Figure 8a) and in the orthoenstatite field ($10^{-5}s^{-1}$ and 1250°C, Figure 8b). The stresses for the two-phase mixtures are calculated using the dislocation creep components of our flow laws, with the uncertainties given as 1σ (Tables 6 and 7). As seen on these figures, the strength of enstatite-olivine aggregates slightly increases as a function of enstatite content, and all the two-phases mixtures have strengths that are between those of pure olivine and pure enstatite. This confirms that in the absence of other dominant deformation mechanisms, the strength of a two-phase mixture is bounded by the strengths of the two end-members.

Theoretical models have been developed for predicting rheologies of mixed-phase aggregates from the rheologies of the end-members similarly to the Voigt and Reuss bounds for elasticity. Assumptions of uniform strain rate (Taylor bound) or uniform stress (Sachs bound) in a viscous polyphase aggregate lead to

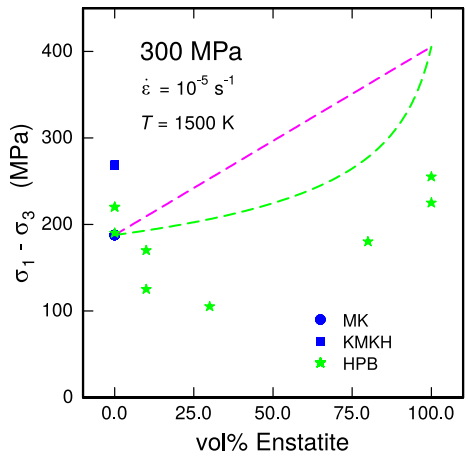

Figure 9. Flow stress versus vol% enstatite at 1227°C (1500 K) and a strain rate of 10^{-5} s^{-1} in enstatite-olivine aggregates deformed in the protoenstatite field. The dashed purple and green lines represent the uniform strain rate (Taylor) and uniform stress (Sachs) bounds, respectively, based on our data for protoenstatite-olivine mixtures. Also shown as green stars are data from Hitchings et al. (1989) on deformation of olivine-protoenstatite under these conditions. The filled blue circle and square represent calculations using the flow laws for olivine aggregates buffered at Ni/NiO from Mei and Kohlstedt (2000b) (MK) and Keefner et al. (2011) (KMKH), respectively.

the determination of rigorous upper or lower bounds for the overall strength of the material (see e.g., Equations 2–6 in Tullis et al., 1991). Taylor and Sachs bounds calculated using the data for the olivine and enstatite end-members are shown in dashed lines in Figures 8a and 8b. In both the protoenstatite and the orthoenstatite field, all the two-phase mixtures have strengths that are essentially within the two bounds, as predicted by theory. As the strength contrast between enstatite and olivine is relatively modest, the bounds are close together and give tight predictions for the strengths of enstatite-olivine aggregates as a function of volume fraction.

Figure 9 shows the enstatite-olivine data from Hitchings et al. (1989), together with the uniform strain rate and stress bounds recalculated from our data at these conditions. As in our study, protoenstatite is stronger than olivine, though the difference in strength is more modest. However, in contrast to us, they observe a decrease in strength at intermediate compositions, although they note that these results may reflect differences in oxygen fugacity in the various samples. Clearly, their data plot outside of the uniform strain rate and stress bounds (whether calculated with our end-member data or theirs), but the lack of systematics in thermochemical environment and in phase composition of their samples makes it difficult to make a robust comparison with our results. Another study by Ji et al. (2001) focused on the strength of iron-free forsterite-enstatite aggregates in the protoenstatite field. Although pure enstatite was weaker than pure forsterite, likely because the forsterite was finer grained than enstatite and deformed by diffusion creep, they observed similar mixing trends as in our study (progressive change in strength, stress exponent, and activation energy as a function of phase proportions).

For reference, Figures 8 and 9 also show the strength of olivine calculated with the dislocation creep flow law obtained from experiments on dry Aheim dunite (Keefner et al., 2011). Figure 8 also includes the single crystal data from Bai et al. (1991), which bracket the aggregate strength data. The Mei and Kohlstedt (2000b) data are clearly weaker than the Keefner et al. (2011) data, consistent with de-emphasis of the strongest slip system (010)[001] during homogeneous aggregate deformation of fine-grained olivine samples. A proposed explanation for this difference in behavior is an increased contribution of grain boundary diffusion and grain boundary sliding processes in fine-grained aggregates (e.g., Hirth & Kohlstedt, 2003). While such processes might result in enhanced weakening in two-phase mixtures relative to the end-member compositions, we see no evidence for this in our enstatite-olivine aggregates.

4.4. Implications for Flow in the Earth

One of the key motivations for this study was to determine the extent to which the addition of a second phase to olivine aggregates would result in differences in mechanical behavior and, hence, in a reevaluation of dynamical models for Earth's interior that have been traditionally based on a simple olivine rheology. The suggestion of possible weakening effects due to the presence of a second phase such as pyroxene (Hitchings et al., 1989) demanded a more robust investigation. Our study shows that olivine and orthoenstatite have similar strengths when deforming by dislocation creep under laboratory conditions. However, the thermomechanical conditions appropriate for the lithosphere and asthenosphere are quite different from those in our experiments. While strain rates in Earth's interior are many orders of magnitude slower than in the laboratory, values of the stress exponent for both olivine and orthopyroxene are essentially the same, such that the contrast in strength in the deep Earth will remain relatively modest. This is illustrated in Figure 10, which shows the extrapolation of the effective viscosities (defined here as $\sigma/2\dot{\varepsilon}$) derived from our rheologies to a strain rate of 10^{-15} s^{-1} for a range of temperatures. The similar activation energies for creep of olivine and orthopyroxene aggregates indicate that both phases will likely have similar strengths under the conditions of the deeper lithosphere and asthenosphere. The contrast in mechanical behavior is even more modest between pure olivine aggregates and a

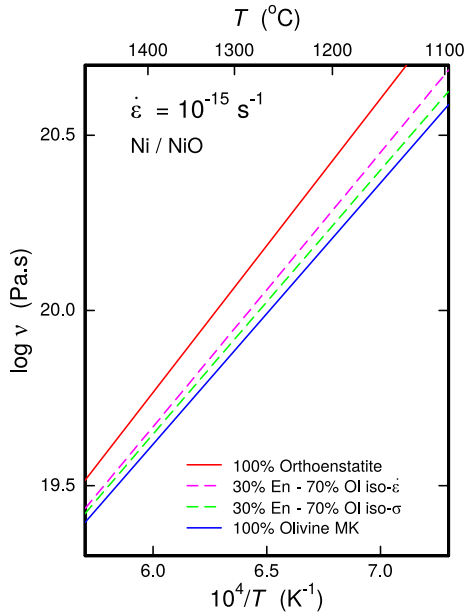

Figure 10. Log of effective viscosity versus temperature at a mantle-relevant strain rate of 10^{-15} s^{-1} for 100 vol% orthoenstatite, 100 vol% olivine, and 30 vol% orthoenstatite—70 vol% olivine, a composition similar to that believed to be appropriate for the lower lithosphere and asthenosphere. The mixed phase dashed lines follow the convention from Figure 8 and show the uniform strain rate (purple) and uniform stress (green) bounds bracketing the viscosity of the olivine-orthoenstatite mixture. The orthoenstatite viscosity is calculated using the flow law presented in Figure 4. The olivine data is from Mei and Kohlstedt (2000b) (MK) for samples deformed under essentially the same conditions as the enstatite and mixed phase data from this study. The curves represent effective viscosities at a confining pressure of 300 MPa; no pressure corrections have been applied for any of the compositions as the activation volume for creep of enstatite is not well constrained.

30 vol% orthopyroxene—70 vol% olivine aggregate, a bulk composition more appropriate for the upper mantle (Figure 10).

Although these results provide some confidence in using rheologies for olivine aggregates as a good proxy for mantle behavior, our experiments only investigated deformation under dry conditions and at low confining pressures relative to those in the deep mantle. While we have fairly robust measurements for the pressure dependence of polycrystalline olivine deformation (e.g., activation volume $V^* = 15 \pm 5$ cm^3/mol, Dixon & Durham, 2018; see also references therein), data for orthopyroxene exist only for oriented enstatite single crystals ($V^* \sim 13.6$ cm^3/mol for the [001] (100) slip system in proto/orthoenstatite, and $V^* \sim 8.3$ cm^3/mol for the [001] (010) slip system in orthoenstatite, Raterron et al., 2016). The activation volume might therefore be somewhat lower for enstatite than for olivine; however a comparison between single crystal and polycrystalline data is not straightforward, and more studies on polycrystalline enstatite at high pressures are needed to assess the effect of pressure on the contrast in mechanical behavior between the two minerals at depth. In addition, dry deformation data is unlikely to be appropriate to Earth's asthenosphere. While studies have quantified the effects of water on deformation of olivine (see e.g., Mei & Kohlstedt, 2000b, and references therein) and orthopyroxene (Zhang et al., 2020), a comparison of the strengths of olivine-pyroxene aggregates under hydrous conditions taking into account the complexities of partitioning of water between olivine and enstatite (Mierdel et al., 2007) is beyond the scope of the present study. It should also be kept in mind that the present study focuses on deformation to low strains, in aggregates where the phases are well mixed. In the lithosphere, microstructural evolution at large strains in polyphase rocks (grain size reduction by dynamic recrystallization, phase separation, etc.) may cause changes in dominant deformation mechanisms, major rheological weakening and shear localization (e.g., de Bresser et al., 2001; Hansen & Warren, 2015; Toy et al., 2010), making the use of uniform strain rate (Taylor) and stress (Sachs) bounds for a well-mixed polyphase aggregate inappropriate.

Data Availability Statement

All the original data presented in this study are available on zenodo.org at Bystricky et al. (2023) https://doi.org/10.5281/zenodo.8172453.

Acknowledgments
We wish to thank Prof. David Kohlstedt for his generous support throughout this research, and Yves Bernabé, Phil Skemer and an anonymous reviewer for their constructive comments on this manuscript. JL and SM are grateful for support from NSF (including EAR-9018044). FH gratefully acknowledges support through DFG Grant He3258/2-1. MB wishes to thank Arnaud Proietti for help with electron microscopy on the starting material at the Plateforme de Microcaractérisation Raimond Castaing (Université de Toulouse, France).

References

Asaadi, N., Ribe, N. M., & Sobouti, F. (2011). Inferring non linear mantle rheology from the shape of the Hawaiian swell. *Nature*, *473*(7348), 501–504. https://doi.org/10.1038/nature09993

Bai, Q., & Kohlstedt, D. L. (1992). High-temperature creep of olivine single crystals, 2. Dislocation structures. *Tectonophysics*, *206*(1–2), 1–29. https://doi.org/10.1016/0040-1951(92)90365-d

Bai, Q., Mackwell, S. J., & Kohlstedt, D. L. (1991). High-temperature creep of olivine single crystals 1. Mechanical Results for buffered samples. *Journal of Geophysical Research*, *96*(B2), 2441–2463. https://doi.org/10.1029/90jb01723

Baptiste, V., Tommasi, A., Vauchez, A., Demouchy, S., & Rudnick, R. (2015). Deformation, hydration, and anisotropy of the lithospheric mantle in an active rift: Constraints from mantle xenoliths from the North Tanzanian Divergence of the East African Rift. *Tectonophysics*, *639*, 34–55. https://doi.org/10.1016/j.lithos.2012.05.001

Becker, T. W., Kustowski, B., & Ekstrom, G. (2008). Radial seismic anisotropy as a constraint for upper mantle rheology. *Earth and Planetary Science Letters*, *267*(1–2), 213–227. https://doi.org/10.1016/j.epsl.2007.11.038

Ben Ismail, W., & Mainprice, D. (1998). An olivine fabric database: An overview of upper mantle fabrics and seismic anisotropy. *Tectonophysics*, *296*(1–2), 145–157. https://doi.org/10.1016/s0040-1951(98)00141-3

Borch, R. S., & Green, H. W., II. (1989). Deformation of peridotite at high pressure in a new molten salt cell: Comparison of traditional and homologous temperature treatments. *Physics of the Earth and Planetary Interiors*, *55*(3–4), 269–276. https://doi.org/10.1016/0031-9201(89)90075-7

Buseck, P. R., Nord, G. L., Jr., & Veblen, D. R. (1980). Chapter 4: Subsolidus phenomena in pyroxenes, *in* Pyroxenes. *Reviews in Mineralogy*, *4*, 117–211.

Bystricky, M., Heidelbach, F., & Mackwell, S. (2006). Large-strain deformation and strain partitioning in polyphase rocks: Dislocation creep of olivine-magnesiowüstite aggregates. *Tectonophysics*, *427*(1–4), 115–132. https://doi.org/10.1016/j.tecto.2006.05.025

Bystricky, M., Kunze, K., Burlini, L., & Burg, J.-P. (2000). High shear strain of olivine aggregates: Rheological and seismic consequences. *Science*, *290*(5496), 1564–1567. https://doi.org/10.1126/science.290.5496.1564

Bystricky, M., Lawlis, J., Mackwell, S., & Heidelbach, F. (2023). Data for the research article "high-temperature deformation of enstatite-olivine aggregates" [Dataset]. Zenodo. https://doi.org/10.5281/zenodo.8172453

Bystricky, M., Lawlis, J., Mackwell, S., Heidelbach, F., & Raterron, P. (2016). High-temperature deformation of enstatite aggregates. *Journal of Geophysical Research: Solid Earth*, *121*(9), 6384–6400. https://doi.org/10.1029/2016JB013011

Bystricky, M., & Mackwell, S. (2001). Creep of dry clinopyroxene aggregates. *Journal of Geophysical Research*, *106*(B7), 13443–13454. https://doi.org/10.1029/2001jb000333

Carter, N. L., & Avé Lallemant, H. G. (1970). High temperature flow of dunite and peridotite. *The Geological Society of America Bulletin*, *81*(8), 2181–2202. https://doi.org/10.1130/0016-7606(1970)81[2181:htfoda]2.0.co;2

Chopra, P. N., & Paterson, M. S. (1981). The experimental deformation of dunite. *Tectonophysics*, *78*(1–4), 453–473. https://doi.org/10.1016/0040-1951(81)90024-x

Chopra, P. N., & Paterson, M. S. (1984). The role of water in the deformation of dunite. *Journal of Geophysical Research*, *89*(B9), 7861–7876. https://doi.org/10.1029/jb089ib09p07861

Coe, R. S., & Kirby, S. H. (1975). The orthoenstatite to clinoenstatite transformation by shearing and reversion by annealing: Mechanism and potential applications. *Contributions to Mineralogy and Petrology*, *52*(1), 29–55. https://doi.org/10.1007/bf00378000

de Bresser, J. H. P., Ter Heege, J. H., & Spiers, C. J. (2001). Grain size reduction by dynamic recrystallization: Can it result in major rheological weakening? *Int. J. Earth Sciences (Geol. Rundsch.)*, *90*(1), 28–45. https://doi.org/10.1007/s005310000149

Dixon, N. A., & Durham, W. B. (2018). Measurement of activation volume for creep of dry olivine at upper-mantle conditions. *Journal of Geophysical Research*, *123*(10), 8459–8473. https://doi.org/10.1029/2018JB015853

Durham, W. B., & Goetze, C. (1977). Plastic flow of oriented single crystals of olivine. *Journal of Geophysical Research*, *83*(36), 5737–5753. https://doi.org/10.1029/jb082i036p05737

Durham, W. B., Mei, S., Kohlstedt, D. L., Wang, L., & Dixon, N. A. (2009). New measurements of activation volume in olivine under anhydrous conditions. *Physics of the Earth and Planetary Interiors*, *172*(1–2), 67–73. https://doi.org/10.1016/j.pepi.2008.07.045

Faul, U. H., Fitz Gerald, J. D., Farla, R. J. M., Ahlefeldt, R., & Jackson, I. (2011). Dislocation creep of fine-grained olivine. *Journal of Geophysical Research*, *116*(B1), B01203. https://doi.org/10.1029/2009JB007174

Frost, H. J., & Ashby, M. F. (1982). *Deformation-mechanism maps: The plasticity and creep of metals and ceramics* (p. 167). Pergamon.

Hansen, L. N., & Warren, J. M. (2015). Quantifying the effect of pyroxene on deformation of peridotite in a natural shear zone. *Journal of Geophysical Research: Solid Earth*, *120*(4), 2717–2738. https://doi.org/10.1002/2014JPB011584

Hansen, L. N., Zimmerman, M. E., & Kohlstedt, D. L. (2011). Grain boundary sliding in San Carlos olivine: Flow law parameters and crystallographic-preferred orientation. *Journal of Geophysical Research*, *116*(B8), B08201. https://doi.org/10.1029/2011JB008220

Hirth, G., & Kohlstedt, D. L. (1995a). Experimental constraints on the dynamics of the partially molten upper mantle: Deformation in the diffusion creep regime. *Journal of Geophysical Research*, *100*(B2), 1981–2001. https://doi.org/10.1029/94jb02128

Hirth, G., & Kohlstedt, D. L. (1995b). Experimental constraints on the dynamics of the partially molten upper mantle, 2. Deformation in the dislocation creep regime. *Journal of Geophysical Research*, *100*, 15441–15449. https://doi.org/10.1029/95jb01292

Hirth, G., & Kohlstedt, D. L. (2003). Rheology of the upper mantle and the mantle wedge: A view from the experimentalists. In J. Eiler (Ed.), *Inside the subduction factory, geophysical monograph 138* (pp. 83–105). AGU.

Hirth, G., & Kohlstedt, D. L. (2015). The stress dependence of olivine creep rate: Implications for extrapolation of lab data and interpretation of rerystallized grain size. *Earth and Planetary Science Letters*, *418*, 20–26. https://doi.org/10.1016/j.epsl.2015.02.013

Hitchings, R. S., Paterson, M. S., & Bitmead, J. (1989). Effects of iron and magnetite additions in olivine-pyroxene rheology. *Physics of the Earth and Planetary Interiors*, *55*(3–4), 277–291. https://doi.org/10.1016/0031-9201(89)90076-9

Huebner, J. S. (1980). Pyroxene phase equilibria at low pressure. In C. T. Prewitt (Ed.), *Pyroxenes, reviews in mineralogy* (Vol. 7, pp. 213–288). Mineral. Soc. America.

Ji, S. C., Wang, Z., & Wirth, R. (2001). Bulk flow strength of forsterite-enstatite composites as a function of forsterite content. *Tectonophysics*, *341*(1–4), 69–93. https://doi.org/10.1016/s0040-1951(01)00191-3

Karato, S., & Jung, H. (2003). Effects of pressure on high-temperature dislocation creep in olivine. *Philosophical Magazine*, *83*(3), 401–414. https://doi.org/10.1080/0141861021000025829

Karato, S., Paterson, M. S., & Fitz Gerald, J. D. (1986). Rheology of synthetic olivine aggregates: Influence of grain size and water. *Journal of Geophysical Research*, *91*, 8151–8179.

Keefner, J. W., Mackwell, S. J., Kohlstedt, D. L., & Heidelbach, F. (2011). Dependence of dislocation creep of dunite on oxygen fugacity: Implications for viscosity variations in Earth's mantle. *Journal of Geophysical Research*, *116*(B5), B05201. https://doi.org/10.1029/2010JB007748

Kirby, S. H., & Kronenberg, A. K. (1987). Rheology of the lithosphere: Selected topics. *Reviews of Geophysics*, *25*(6), 1219–1244. https://doi.org/10.1029/rg025i006p01219

Kohlstedt, D. L., Evans, B., & Mackwell, S. J. (1995). Strength of the lithosphere: Constraints imposed by laboratory experiments. *Journal of Geophysical Research*, *100*(B9), 17587–17602. https://doi.org/10.1029/95jb01460

Mackwell, S. J. (1991). High-temperature rheology of enstatite: Implications for creep in the mantle. *Geophysical Research Letters*, *18*(11), 2027–2030. https://doi.org/10.1029/91gl02492

Mainprice, D., & Silver, P. G. (1993). Interpretation of SKS-waves using samples from the subcontinental lithosphere. *Physics of the Earth and Planetary Interiors*, *78*(3–4), 257–280. https://doi.org/10.1016/0031-9201(93)90160-b

Mainprice, D., Tommasi, A., Couvy, H., Cordier, P., & Frost, D. J. (2005). Pressure sensitivity of olivine slip systems and seismic anisotropy of Earth's upper mantle. *Nature*, *433*(7027), 731–733. https://doi.org/10.1038/nature03266

McDonnell, R. D., Peach, C. J., van Roermund, H. L. M., & Spiers, C. J. (2000). Effect of varying enstatite content on the deformation of fine-grained synthetic peridotite under wet conditions. *Journal of Geophysical Research*, *105*(B6), 13535–13553. https://doi.org/10.1029/1999jb900412

Mei, S., & Kohlstedt, D. L. (2000a). Influence of water on plastic deformation of olivine aggregates. 1. Diffusion creep regime. *Journal of Geophysical Research*, *105*(B9), 21457–21469. https://doi.org/10.1029/2000jb900179

Mei, S., & Kohlstedt, D. L. (2000b). Influence of water on plastic deformation of olivine aggregates. 2. Dislocation creep regime. *Journal of Geophysical Research*, *105*(B9), 21471–21481. https://doi.org/10.1029/2000jb900180

Mierdel, K., Keppler, H., Smyth, J. R., & Langenhorst, F. (2007). Water solubility in aluminous orthopyroxene and the origin of earth's asthenosphere. *Science*, *315*(5810), 364–368. https://doi.org/10.1126/science.1135422

Montagner, J.-P. (1998). Where can seismic anisotropy be detected in the Earth's mantle? In boundary layers. *Pure and Applied Geophysics*, *151*(4), 223–256. https://doi.org/10.1007/s000240050113

Nicolas, A., & Christensen, N. I. (1987). Formation of anisotropy in upper mantle peridotites – A review. *Composition, Structure and Dynamics of the Lithosphere-Asthenosphere System*, *16*, 111–123.

Ohuchi, T., Kawazoe, T., Higo, Y., & Suzuki, A. (2017). Flow behavior and microstructures of hydrous olivine aggregates at upper mantle pressures and temperatures. *Contributions to Mineralogy and Petrology*, *172*(8), 65. https://doi.org/10.1007/s00410-017-1375-8

Paterson, M. S. (1987). Problems in the extrapolation of laboratory rheological data. *Tectonophysics*, *133*(1–2), 33–43. https://doi.org/10.1016/0040-1951(87)90278-2

Paterson, M. S. (2001). Relating experimental and geological rheology. *International Journal of Earth Sciences*, *90*(1), 157–167. https://doi.org/10.1007/s005310000158

Paterson, M. S., & Chopra, P. N. (1982). The jacketing of specimens in high-temperature, high-pressure rock-deformation experiments. *High Temperatures - High Pressures*, *14*, 315–318.

Paterson, M. S. (1990). Rock deformation experimentation. In A. G. Duba, et al. (Eds.), *Brittle-ductile transition in rocks*, *Geophys. Monogr. Ser.* (Vol. 56, pp. 187–194). AGU.

Poirier, J.-P. (1985). *Creep of crystals* (p. 260). Cambridge Univ. Press.

Précigout, J., & Stünitz, H. (2016). Evidence of phase nucleation during olivine diffusion creep field: A new perspective for mantle strain localisation. *Earth and Planetary Science Letters*, *455*, 94–105. https://doi.org/10.1016/j.epsl.2016.09.029

Raleigh, C. B., Kirby, S. H., Carter, N. L., & Avé Lallemant, H. G. (1971). Slip and clinoenstatite transformation as competing rate processes in enstatite. *Journal of Geophysical Research*, *76*(17), 4011–4022. https://doi.org/10.1029/jb076i017p04011

Raterron, P., Fraysse, G., Girard, J., & Holyoke, C., III. (2016). Strength of orthoenstatite single crystals at mantle pressure and temperature and comparison with olivine. *Earth and Planetary Science Letters*, *450*, 326–336. https://doi.org/10.1016/j.epsl.2016.06.025

Ross, J. V., & Nielsen, K. C. (1978). High-temperature flow of wet polycrystalline enstatite. *Tectonophysics*, *44*(1–4), 233–261. https://doi.org/10.1016/0040-1951(78)90072-0

Silver, P., Mainprice, D., Ben Ismail, W., Tommasi, A., & Barruol, G. (1999). Mantle structural geology from seismic anisotropy, mantle petrology: Field observations and high pressure experimentation: A tribute to Francis R. (Joe) Boyd (Vol. *6*, pp. 79–103).

Smith, G. P., & Eckström, G. (1999). A global study of P_n anisotropy beneath continents. *Journal of Geophysical Research: Solid Earth*, *104*(B1), 963–980. https://doi.org/10.1029/1998jb900021

Soustelle, V., & Manthilake, G. (2017). Deformation of olivine-orthopyroxene aggregates at high pressure and temperature: Implications for the seismic properties of the asthenosphere. *Tectonophysics*, *694*, 385–399. https://doi.org/10.1016/j.tecto.2016.11.020

Sundberg, M., & Cooper, R. F. (2008). Crystallographic preferred orientation produced by diffusional creep of harzburgite: Effects of chemical interactions among phases during plastic flow. *Journal of Geophysical Research*, *113*(B12), B12208. https://doi.org/10.1029/2008JB005618

Tasaka, M., Hiraga, T., & Zimmerman, M. E. (2013). Influence of mineral fraction on the rheological properties of forsterite + enstatite during grain-size-sensitive creep: 2. Deformation experiments. *Journal of Geophysical Research*, *118*(8), 3991–4012. https://doi.org/10.1002/jgrb.50284

Tasaka, M., Zimmerman, M. E., & Kohlstedt, D. L. (2017). Rheological weakening of olivine + orthopyroxene aggregates due to phase mixing: 1. Mechanical behavior. *Journal of Geophysical Research*, *122*(10), 7584–7596. https://doi.org/10.1002/2017JB014333

Tasaka, M., Zimmerman, M. E., & Kohlstedt, D. L. (2020). Rheological weakening of olivine + orthopyroxene aggregates due to phase mixing: Effects of orthopyroxene volume fraction. *Journal of Geophysical Research*, *125*(9), e2020JB019888. https://doi.org/10.1029/2020JB019888

Ter Heege, J. H., de Bresser, J. H. P., & Spiers, C. J. (2004). Composite flow laws for crystalline materials with log-normally distributed grain size: Theory and application to olivine. *Journal of Structural Geology*, *26*, 1693–1705. https://doi.org/10.1016/s0191-8141(04)00028-8

Tommasi, A., & Vauchez, A. (2015). Heterogeneity and anisotropy in the lithospheric mantle. *Tectonophysics*, *661*, 11–37. https://doi.org/10.1016/j.tecto.2015.07.026

Toy, V. G., Newman, J., Lamb, W., & Tikoff, B. (2010). The role of pyroxenites in formation of shear instabilities in the mantle: Evidence from an ultramafic ultramylonite, Twin Sisters, Massif, Washington. *Journal of Petrology*, *51*(1–2), 55–80. https://doi.org/10.1093/petrology/egp059

Tullis, T. E., Horowitz, F. G., & Tullis, J. (1991). Flow laws of polyphase aggregates from end-member flow laws. *Journal of Geophysical Research*, *96*(B5), 8081–8096. https://doi.org/10.1029/90jb02491

Van Duysen, J. C., Doukhan, N., & Doukhan, J. C. (1985). Transmission electron microscope study of dislocations in orthopyroxene $(Mg, Fe)_2Si_2O_6$. *Physics and Chemistry of Minerals*, *12*(1), 39–44. https://doi.org/10.1007/bf00348745

van Hunen, J., Zhong, S., Shapiro, N. M., & Ritzwoller, M. H. (2005). New evidence for dislocation creep from 3-D geodynamic modeling of the Pacific upper mantle structure. *Earth and Planetary Science Letters*, *238*(1–2), 146–155. https://doi.org/10.1016/j.epsl.2005.07.006

Wang, J. N. (1994). The effect of grain size distribution on the rheological behavior of polycrystalline materials. *Journal of Structural Geology*, *16*(7), 961–970. https://doi.org/10.1016/0191-8141(94)90078-7

Zaffarana, C., Tommasi, A., Vauchez, A., & Grégoire, M. (2014). Microstructures and seismic properties of south Patagonian mantle xenoliths (Gobernador Gregores and Pali Aike). *Tectonophysics*, *621*, 175–197. https://doi.org/10.1016/j.tecto.2014.02.017

Zeuch, D. H., & Green, H. W. (1984). Experimental deformation of a synthetic dunite at high temperature and pressure 1. Mechanical behavior, optical microstructure and deformation mechanisms. *Tectonophysics*, *110*(3–4), 233–262. https://doi.org/10.1016/0040-1951(84)90263-4

Zhang, G., Mei, S., & Song, M. (2020). Effect of water on the dislocation creep of enstatite aggregates at 300 MPa. *Geophysical Research Letters*, *47*(5), e2019GL085895. https://doi.org/10.1029/2019GL085895

Zhang, G., Mei, S., Song, M., & Kohlstedt, D. L. (2017). Diffusion creep of enstatite at high pressures under hydrous conditions. *Journal of Geophysical Research: Solid Earth*, *122*(10), 7718–7728. https://doi.org/10.1002/2017JB014400

Zhao, N., Hirth, G., Cooper, R. F., Kruckenberg, S. C., & Cukjati, J. (2019). Low viscosity of mantle rocks linked to phase boundary sliding. *Earth and Planetary Science Letters*, *517*, 83–94. https://doi.org/10.1016/j.epsl.2019.04.019